Remote Sensing Applications: Society and Environment 37 (2025) 101438

Contents lists available at ScienceDirect

Remote Sensing Applications: Society and Environment

journal homepage: www.elsevier.com/locate/rsase

Error-reduced digital elevation models and high-resolution land cover roughness in mapping tsunami exposure for low elevation coastal zones

Rajuli Amra [a,*], Susumu Araki [a], Christian Geiß [b,c], Gareth Davies [d]

[a] Department of Civil Engineering, Osaka University, 2-1 Yamadaoka, Suita, Osaka 565-0871, Japan
[b] German Aerospace Center (DLR), German Remote Sensing Data Center (DFD), Münchner Straße 20, 82234, Weßling, Germany
[c] University of Bonn, Department of Geography, Meckenheimer Allee 166, 53115, Bonn, Germany
[d] Community Safety Branch, Geoscience Australia, ACT, Canberra, 2601, Australia

ARTICLE INFO

Keywords:
Error-reduced DEMs
Land cover roughness
Satellite-derived exposure data

ABSTRACT

This study presents a systematic exposure assessment by reconstructing the impact of the 2004 Indian Ocean Tsunami using a wide range of inundation scenarios and multiresolution exposure layers. To develop inundation and exposure models, we employed the error-reduced global digital elevation models (DEMs) and geospatially consistent multiresolution datasets: land cover roughness (LCR) models, built-up areas, and gridded population layers. We implemented three sequential validation assessments to evaluate the performance of inundation models, incorporating satellite observations, post-tsunami measurements, and the confidence level associated with inherent DEM error characteristics. The results demonstrated that the error-reduced variants of Copernicus DEM (i.e., FABDEM and DiluviumDEM) satisfied all reliability criteria. Incorporating these elevation models with LCR models improved the accuracy of inundation depth estimates; however, it reduced the agreement between simulated and observed inundation extents. We observed that applying high-resolution LCR models had a minimal impact on overland inundation extents but still influenced the exposure assessment, especially in high-density urban areas.

1. Introduction

Mapping hazard exposure is vital for disaster preparedness of infrequent but potentially devastating hazards such as tsunamis. To quantify assets and populations at tsunami risk, information on tsunami inundation, built-up areas, and population distributions is required (Behrens et al., 2021). A hazard map, which provides information on the spatial extent of inundated areas, can be derived from satellite observations of past events and numerical inundation modeling (Bernhofen et al., 2022). Satellite observations can provide a rapid assessment of inundation extents. However, this method cannot comprehensively characterize the potential for inundation in future events with different tsunami source characteristics (Schumann, 2021). Additionally, inundation is sensitive to topographical features that might change after a tsunami disaster (Gibbons et al., 2022; Liu et al., 2021; Griffin et al., 2015). Hence, an overemphasis on satellite-observed historical inundation might introduce bias, especially for long-term tsunami exposure assessment.

* Corresponding author.
E-mail address: rajuliamra@civil.eng.osaka-u.ac.jp (R. Amra).

https://doi.org/10.1016/j.rsase.2024.101438
Received 26 September 2024; Received in revised form 1 December 2024; Accepted 16 December 2024
Available online 18 December 2024

Unlike satellite observations, inundation models can account for the effects of terrain attributes on inundation hazards (Fukui et al., 2022). McClean et al. (2020) found that high-resolution topographic data from airborne light detection and ranging (LiDAR) can represent the terrain features well enough to support detailed inundation maps. However, the availability of LiDAR data is limited, and so most inundation hazard assessments rely on "best-available" elevation datasets, including the global digital elevation models (DEMs) (Hawker et al., 2018). Unfortunately, global DEMs contain many errors, potentially leading to inaccurate inundation estimates. For example, the widely used Shuttle Radar Topography Mission (SRTM) (Farr et al., 2007) tends to underestimate the inundation extent and consequently underrepresent the population exposed to coastal flooding (Hinkel et al., 2021). This underestimation may be caused by SRTM-associated errors, e.g., vertical and vegetation bias (Yamazaki et al., 2017).

Recently, several studies have been conducted to address the inherent biases of SRTM. These studies have resulted in improved variants of SRTM, including NASADEM (NASA JPL, 2020), CoastalDEM (Kulp and Strauss, 2018), and multi-error-removed improved terrain DEM (MERIT) (Yamazaki et al., 2017). The latter was developed by combining information from SRTM and ALOS World 3D – 30 m (AW3D30) (Tadono et al., 2016). In addition to SRTM, efforts to reduce errors in a relatively newly released global DEM, the Copernicus DEM – 30 m (COP30) (Fahrland et al., 2022), resulted in two other enhanced variants: the forest and building removed DEM (FABDEM) (Hawker et al., 2022) and DiluviumDEM (Dusseau et al., 2023). We referred to these improved elevation datasets as error-reduced DEMs. To the best of our knowledge, applications of error-reduced DEMs are still limited to sea-level rise projections (Seeger et al., 2023; Dusseau et al., 2023). This highlights the need to investigate the performance of these new DEMs within broader coastal flooding applications, including tsunami inundation.

In the absence of high-resolution topographic data, the effects of terrain attributes could also be represented by combining "bare-earth" topography (buildings and vegetation elevation are removed) with surface roughness coefficients (Gibbons et al., 2022; Sadashiva et al., 2022). These coefficients are represented by Manning's n values, which can be spatially uniform or vary based on the land cover maps, also known as land cover roughness (LCR) models. Previous studies suggested that a high-resolution LCR model could yield more accurate inundation results (Kaiser et al., 2011; Gayer et al., 2010). However, the extent to which the spatial resolution of LCR models affects inundation estimates has not been examined comprehensively. Although Laso Bayas et al. (2015) have investigated the effect of variable LCR models derived from multiresolution land cover maps on tsunami simulations, the high cloud coverage in satellite imagery used to generate the land cover maps hindered a definitive conclusion.

In addition to the challenges in accurately modelling the inundation extent, the characteristics of exposure data (i.e., input data, methodology, spatial and temporal resolution) also influence the inundation exposure assessment (Behrens et al., 2021). Following the development of the earth observation system, many global scale exposure datasets are publicly accessible, including land cover maps,

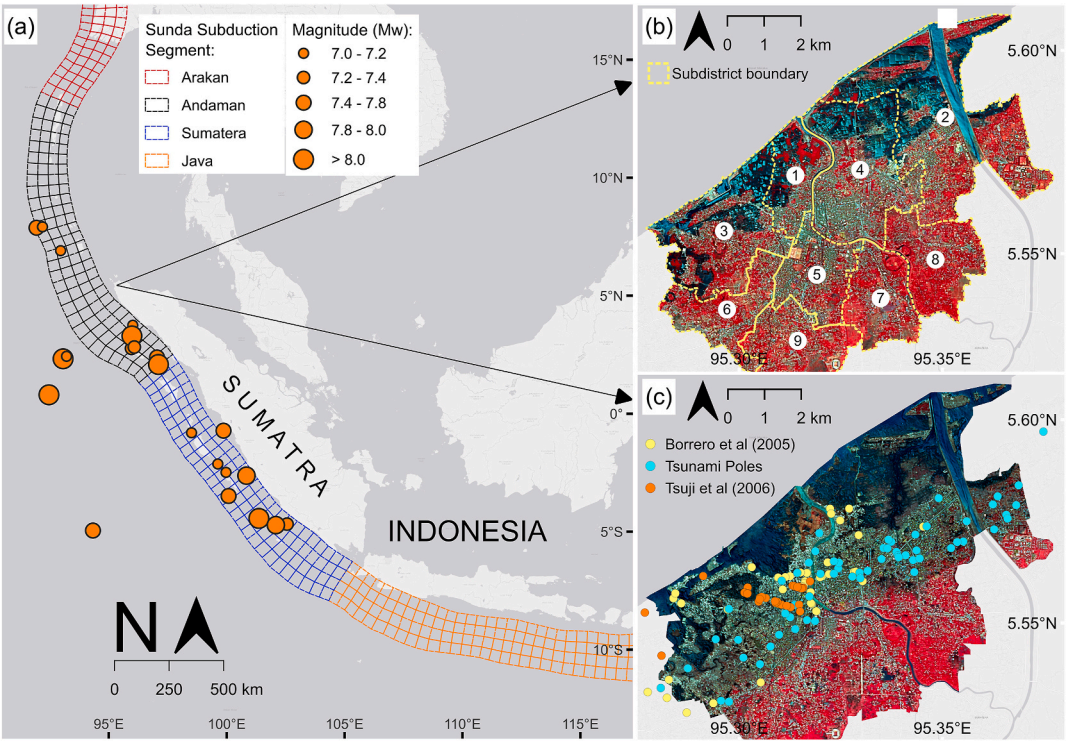

Fig. 1. (a) The tectonic setting and historical earthquake distribution (Mw > 7) in Sunda Subduction (Davies and Griffin, 2020; U.S. Geological Survey, 2024) (Basemap: ESRI Light Gray). (b) Banda Aceh before the 2004 IOT. The circled numbers and dashed yellow lines indicate the IDs and boundaries of subdistricts (https://gadm.org) (Basemap: SPOT 5 05-08-2004). (c). Banda Aceh after the 2004 IOT. Coloured markers indicate the distributions of post-tsunami measurement data. (Basemap: SPOT 5 29-01-2005).

built-up layers, and gridded population datasets (Table S1 of the Supplementary File). Nonetheless, employing these exposure datasets for local-scale tsunami assessment may introduce bias due to their low resolution, geolocation misalignment across datasets, and inconsistencies in methodology (Bernhofen et al., 2022; Sleeter et al., 2017).

Given these limitations, this study aimed to investigate the performance of error-reduced DEMs, paired with multiresolution LCR models, in modeling tsunami inundation in our area of interest (AOI). The AOI is in Banda Aceh, a major coastal city at the northern tip of Sumatra, Indonesia (Fig. 1). Banda Aceh, which encompasses nine subdistricts (Fig. 1b), is a low-lying coastal plain with a typical elevation of less than 10 m above sea level (Meilianda et al., 2019). The city is situated along the tectonically active Sunda-Andaman subduction zone and was heavily affected by the 2004 Indian Ocean Tsunami (IOT).

We numerically reconstructed the 2004 IOT inundation using a finite fault model of Koshimura et al. (2009). The simulated inundation extents were compared against satellite observations in 2004, while the inundation depth estimates were validated against field measurement data. The measured data were collected from various sources, including Tsuji et al. (2006), Borrero (2005), and tsunami poles (Sugimoto et al., 2010), as shown in Fig. 1c. To assess the potential impacts, the simulated inundation extents were intersected with exposure variables. We applied the satellite-derived exposure data (SDED) framework, leveraging multiresolution satellite images before and after the 2004 IOT event on December 26, 2004, to develop geospatially consistent high-resolution LCR models and exposure datasets, including built-up and gridded population layers. However, this study does not discuss the detailed inundation aspects, such as tsunami flow around buildings, momentum flux, and time of tsunami arrival.

2. Dataset and methods

2.1. Satellite-derived exposure data (SDED)

SDED involves several interrelated processes: pre-processing of satellite images, land cover classification, creating land cover roughness maps, and generating built-up and gridded population layers. A detailed pipeline is shown in Fig. S1 of the Supplementary File.

2.1.1. Pre-processing of satellite images

We utilized cloud-free multiresolution and multitemporal images from different sensors, as listed in Table 1. The 30 m resolution Landsat data were retrieved from Collection 2 and Level 2 products, which had been geometrically and atmospherically corrected at the surface reflectance level (Crawford et al., 2023). However, the SPOT 5 images, accessed from the SPOT World Heritage (SWH) program, were in Level 1 format and required additional calibration through orthorectification and atmospheric correction (Nosavan et al., 2020). The calibration was carried out using the Python extension of Orfeo Toolbox (pyOTB) (Grizonnet et al., 2017). The SPOT 5 sensor provided multispectral images at 10 m resolution and a panchromatic band at 5 m resolution. We performed a pansharpening process to increase the resolution of multispectral images to 5 m. Overall, we used four input images for the land cover classification process with resolutions of 30 m, 10 m, and 5 m, covering two distinct periods before and after the 2004 IOT (Fig. 2a–d).

To ensure spatial alignment across the input images, we performed image co-registration using AROSICS, a robust and automated co-registration algorithm for multisensor data (Scheffler et al., 2017). We used around 1000 tie points to calculate the maximum shift between the reference (Landsat 5 TM scene) and target images (SPOT 5 scenes). We then compared geolocation offsets before and after co-registration to evaluate the improvement in geolocation accuracy.

To minimize radiometric inconsistencies, we performed radiometric normalization using an iterative reweighted multivariate alteration detection (IR-MAD) transformation (Leach et al., 2019). IR-MAD transformation identifies the invariant pixels between the reference and target images, with a no-change probability threshold of 95% applied for invariant pixel selection. These invariant pixels are then used in a regression model to transform the radiometry of target image to match the reference image. Leach et al. (2019) highlighted that IR-MAD performed better when the acquisition gap between the reference and target images was minimal, e.g., a few months. Given this, we included the 30 m Landsat 8 OLI scene in 2014 (Fig. 2e) as the reference for the 2014 SPOT 5 dataset, while the

Table 1
Satellite image dataset (acquisition time format: yy/mm/dd).

Sensor	Dataset ID an Acquisition (yy/mm/dd)	Band wavelengths/resolutions	Level
Landsat-5 TM	LT51310562004356BKT00	NIR: 760–900 nm/(30 m)	Geometry:
Level-2 Collection 2 (Crawford et al., 2023)	(04/12/21)	Red: 630–690 nm/(30 m)	*Orthorectified*
		Green: 520–600 nm/(30 m)	Radiometry:
		SWIR: 1550–1750 nm/(30 m)	*Surface Reflectance*
Landsat-8 OLI	LC81310562014047LGN01	NIR: 850–880 nm/(30 m)	Geometry:
Level-2 Collection 2 (Crawford et al., 2023)	(14/02/16)	Red: 640–670 nm/(30 m)	*Orthorectified*
		Green: 530–590 nm/(30 m)	Radiometry:
		SWIR: 1570–1650 nm/(30 m)	*Surface Reflectance*
SPOT-5	004-S5-255-339 (04/08/05)	NIR: 780–890 nm/(10 m)	Geometry:
SWH Level 1C (Nosavan et al., 2020)	005-S5-255-339 (04/08/05)	Red: 630–690 nm/(10 m)	*Raw*
	004-S5-255-339 (05/01/29)	Green: 520–600 nm/(10 m)	
	006-S5-255-339 (05/01/29)	SWIR: 1550–1750 nm/(20 m)	Radiometry:
	004-S5-255-339 (14/05/18)	PAN: 1550–1750 nm/(5 m)	*Raw*
	005-S5-255-339 (14/05/18)		

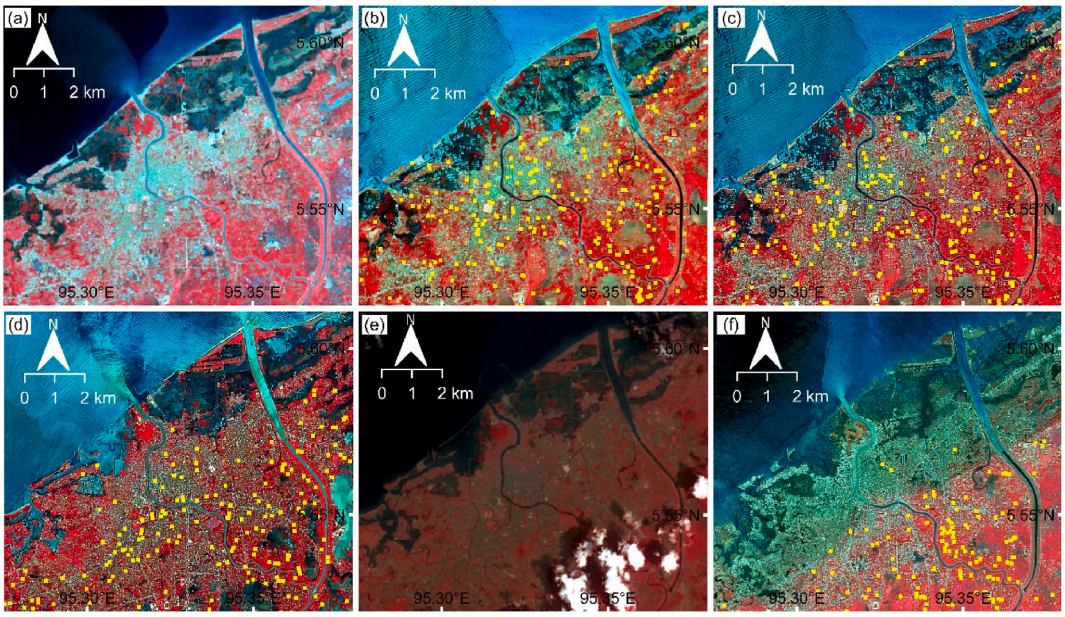

Fig. 2. The image datasets for land cover classification (a) Landsat 5 TM – 30 m 2004, (b) SPOT 5–10 m 2004, (c) SPOT 5–5 m 2004, (d) SPOT 5–5 m 2014, (e) Landsat 8 OLI – 30 m 2014 served as radiometric reference for SPOT 5–5 m 2014, and (f) SPOT 5–5 m 2005 to benchmark the 2004 IOT inundation limit. The yellow dots indicate invariant pixels between reference and target images.

2004 Landsat 5 TM scene served as a reference for the 2004 SPOT 5 images. The radiometric consistency was evaluated by comparing the Normalized Difference Vegetation Index (NDVI) of invariant pixels before and after the normalization process.

2.1.2. Satellite-derived inundation limit

To benchmark the 2004 IOT inundation extent, we utilized the post-disaster imagery from the SPOT 5 scene acquired on January 29, 2005 (Fig. 2f). This image (SPOT 5–5 m 2005) was co-registered and normalized to the 2004 Landsat 5 TM scene. To determine the inundated areas, we integrated manual digitization with a semi-automated approach. The semi-automated method involved generating a Normalized Difference Water Index (NDWI) difference layer, derived from pre-disaster (SPOT 5–5 m 2004) and post-disaster images, and applying a trial-and-error thresholding technique to classify inundated pixels (Koshimura et al., 2020). Next, we performed a post-classification process by manually digitizing areas missed or incorrectly classified by the semi-automated approach. This combined approach can minimize bias in defining inundated extent.

2.1.3. Land cover classification

The land cover classification employed Object-Based Image Analysis with a supervised Random Forest algorithm (OBIA-RF) as the classification technique. Given sufficient prior knowledge (i.e., labelled samples), OBIA-RF is considered a valid approach for land cover mapping (Hermosilla et al., 2022; Geiβ et al., 2017). Image classification was implemented using pyOTB, involving image segmentation, zonal statistics, model training, and image classification. Following Teluguntla et al. (2018), we manually annotated ground truth points using photointerpretation techniques of Google Earth Pro historical imagery. To closely match the acquisition dates of input satellite images, we selected two images in June 2004 and June 2024 and annotated approximately 3000 random points for each dataset (Fig. S2).

The annotated points were divided into five land cover classes: water, bare, low-vegetation, high-vegetation, and built-up areas. To ensure accurate label assignment, we screened the labelled points using the spectral indices listed in Table 2 (Zheng et al., 2021). In

Table 2
List of spectral indices used.

Indices	Formulation	Mapping application
Normalized difference vegetation index (NDVI)	$\frac{NIR - Red}{NIR + Red}$	Vegetation
Normalized difference water index (NDWI)	$\frac{Green - NIR}{Green + NIR}$	Water
Normalized difference built-up index (NDBI)	$\frac{SWIR - NIR}{SWIR + NIR}$	Built-up areas
Second Modified Soil Adjusted Vegetation Index (MSAVI2)	$\frac{2\,x\,NIR + 1 - \sqrt{(2\,x\,NIR + 1)^2 - 8\,x\,(NIR - Red)}}{2}$	Soil

addition to four spectral bands from each input image, these spectral indices bands were then included as additional input features to improve the classification accuracy (Zeferino et al., 2020). All indices' values were rescaled to range between −1 and 1. The description of land cover classes and screening procedures is provided in Table S2 of the Supplementary File.

Next, the ground truth points were fused with polygons resulting from image segmentation to develop the labelled polygon samples. To account for the uneven sample distribution across land cover classes, we applied a proportional class-weighted sampling approach and selected 70% of labelled polygons as training datasets. The remaining 30% of labelled polygons served as validation sets to evaluate classification accuracy. We utilized three accuracy indicators derived from the confusion matrix: overall accuracy, F1 weighted score, and kappa index. To optimize the classification performance, we adopted a grid search method from Python's Scikit-learn (Version 1.5) to select the optimal classification parameters (Liao et al., 2024). Table S3 of the Supplementary File lists the optimum parameters.

We performed a post-classification processing to minimize potential misclassification between built-up and bare classes owing to similarities in the spectral characteristics (Geiβ et al., 2017). Overall, the classification resulted in the 2004 land cover maps at resolutions of 30 m (LC04-30), 10 m (LC04-10), and 5 m (LC04-5), and a land cover map of 2014 at 5 m resolution (LC14-5). To compare our classification results with global data, we carried out an area-based comparison of LC14-5 and GLC-2015. GLC-2015 is a global land cover map developed by fusing multi land cover datasets in 2014 with overall accuracy of 83.6% (Li et al., 2023).

2.1.4. Land cover roughness (LCR) model

To develop the LCR model, we assigned a Manning's n value to each land-cover class based on coefficients in Table S4 of the Supplementary File. Bricker et al. (2015) noted that the widely used Manning coefficients underestimated the dampening effect of dense vegetation and were not sufficient to model tsunami flow in urban areas. Therefore, this study adopted the roughness coefficients derived from large-scale experiments and field measurements. To account for the effect of roughness coefficient variations on the tsunami estimates, we employed two different sets of roughness coefficient provided by Bunya et al. (2010) and Koshimura et al. (2009).

Both studies provide density-based Manning coefficients for built-up areas. We determined the density of built-up areas by calculating the ratio of built-up pixels to total pixels within a 1-ha area. The density of built-up areas was then classified into low (ratio: less than 30%), moderate (ratio: between 30% and 70%), and high-density (ratio: more than 70%). We generated eight LCR models, covering three different spatial resolutions (30 m, 10 m, and 5 m), two distinct periods (2004 and 2014), and two different sources of roughness coefficients.

2.1.5. Exposure variables: built-up and gridded population layers

To develop built-up layers, we extracted the built-up class from each land cover map within Banda Aceh administrative boundary. The built-up layers were then intersected with the subdistrict polygons to create gridded population layers. Following the work of Swanwick et al. (2022), we disaggregated the population data at subdistrict level (Table S5) by calculating the population-to-built-up pixel ratio for each subdistrict. We then assigned the calculated ratio to each built-up pixel. Non-built-up pixels were set to zero.

Some studies narrowly defined the built-up class to exclusively include buildings, aiming for a more granular exposure dataset at the building level (Bonatz et al., 2024). This finer classification enables more detailed population disaggregation (Tiecke et al., 2017). However, using population datasets at building level might introduce an oversimplification, as people may not always be inside the buildings during tsunami events. Therefore, this study employed a wider definition of built-up areas, encompassing all man-made surfaces such as roads, buildings, and impervious surfaces. This wider definition can better reflect distribution of human activity.

We created one set of built-up and gridded population layers at 5 m resolution for the 2014 epoch (BU14-5 and POP14-5). For 2004, we generated multiresolution exposure datasets at resolutions of 30 m (BU04-30 and POP04-30), 10 m (BU04-10 and POP04-10), and 5 m (BU04-5 and POP04-5). To validate the generated exposure layers, we compared total area and population estimates with global

Table 3
List of digital elevation model (DEMs).

DEM (resolution)	Datum	Sensor	Acquisition year and improvement
Original DEMs			
AW3D30 (30 m)	EGM96	Optical stereoscopic	2006 to 2011
COP30 (30 m)	EGM08	SAR interferometry	2010 to 2015
EDEM (30 m)	WGS84	SAR interferometry	2011 to 2015
SRTM (30 m)	EGM96	SAR interferometry	2000
Error reduced DEMs			
CRAWDEM (30 m)	WGS84	EDEM	Added new data from 2017 to 2021
DiluviumDEM (30 m)	EGM08	COP30	Reduced vertical bias
FABDEM (30 m)	EGM08	COP30	Removed building and vegetation biases
NASADEM (30 m)	EGM96	SRTM	Void filling
CoastalDEM (90 m)	EGM96	SRTM & NASADEM	Reduced vertical bias
MERIT (90 m)	EGM96	SRTM & AW3D30	Reduced speckle, stripe, void, and vegetation bias
Local DEM			
DEMNAS (8 m)	EGM08	TERRASAR, IFSAR, and stereo-plotting mass points	

datasets, both within the entire Banda Aceh region and the 2004 IOT inundation extent. The data resolutions were not resampled since no pixel-level analysis was performed. The area estimates from BU14-5 were compared against the 30 m Global Impervious Surface Area (GISA) (Huang et al., 2022). GISA was developed by fusing and improving the consistency of several global datasets to create a long-series of built-up information between 1972 and 2019, with an average F1 score of 0.93. Meanwhile, the population estimates from POP14-5 were compared with the 30 m High-Resolution Settlement Layer (HRSL) (Tiecke et al., 2017). HRSL equally allocated population estimates from the Gridded Population of the World collection version 4 (GPWv4) to human settlement data within the municipalities or district levels.

2.2. DEM error analysis

The error-reduced DEMs varied in their error-removal techniques, acquisition periods, and spatial resolutions, ranging from 30 m to 90 m (Table 3). Previously, Seeger et al. (2023) and Chen et al. (2022) comprehensively analyzed the error characteristics of error-reduced DEMs, except for DiluviumDEM. However, terrain variations can lead to geographically specific error patterns (Hawker et al., 2018). To address this, we performed an elevation error analysis within our research location, before incorporating these data into inundation models. Errors were defined as differences in elevation between the DEMs and the ground truth data (Dusseau et al., 2023). To avoid bias in error interpretation, we employed three statistical measures, including the mean error (ME), mean absolute error (MAE), and root mean square error (RMSE).

Given the unavailability of local LiDAR data, we utilized the ground truth elevations from global altimetry data of ICESat-2 (version 006), acquired from the National Snow and Ice Data Center (https://nsidc.org). ICESat-2 offers several products, including geolocated photon of ATL03 (Neumann et al., 2023) and a land and vegetation height product (ATL08) (Neuenschwander et al., 2023), with along-track resolutions of 20 m and 100 m, respectively. We used Python implementations of the photon research and engineering analysis library (PhoReal) to classify ATL03 photon signals into noise, canopy, and ground elevation data, leveraging labelled information from ATL08 products (Neuenschwander and Magruder, 2023). We downloaded 40 ICESat-2 tracks covering our AOI from December 2018 to June 2023 (Fig. S3 of the Supplementary File). Before error analysis, all DEMs and ICESat-2 data were transformed into the same vertical datum of EGM2008. By leveraging information from the 2014 land cover map, we examined the DEM error patterns across different land cover types: all classes (except water), built-up areas, and highly vegetated regions (forest). Given the topographical characteristics of Banda Aceh region, the error analysis focused on elevations lower than 10 m, a threshold to delimit the low-elevation coastal zone (Gesch, 2018). Details of the analysis workflow are shown in Fig. S4 of the Supplementary File.

In addition to the variants from SRTM, COP30, and AW3D30, we included the TANDEM change elevation data (CRAWDEM) with a resolution of 30 m (Lachaise and Schweiβhelm, 2023). CRAWDEM was developed by incorporating new sensing data (2017–2020) into the 30 m Edit TANDEM (EDEM) dataset (Gonzalez and Bueso-Bello, 2023). We also evaluated the DEMNAS elevation model, a local DEM with a resolution of 8 m launched in 2018 (tanahair.indonesia.go.id). DEMNAS utilized multisource datasets, including IFSAR (5 m), TERRASAR-X (95 m), and ALOS PALSAR (11.25 m), along with additional mass point data obtained from a stereo-plotting operation. However, information regarding the acquisition period of these dataset was limited. Overall, we performed an error analysis for 11 elevation models, including one local DEM, four original DEMs, and six error-reduced variants (Fig. S5).

2.3. Numerical inundation modeling

We simulated the Mw 9.2 2004 IOT using the inversion fault model developed by Koshimura et al. (2009). Fig. S6 and Table S6 of the Supplementary File provide details of fault parameters and initial sea-surface deformation. The simulation was carried out using the Cornell multigrid coupled tsunami model (COMCOT), which solves both the linear and nonlinear two-dimensional shallow water equations (2D-SWE) (Wang and Power, 2011). We utilized four nested domains to model the tsunami from the Sunda-Andaman segment to Banda Aceh region. Table 4 lists the configurations of numerical models.

The outermost domain (Layer 1) with a grid resolution of 1080 m used the initial sea surface deformation as the initial condition, whereas the inner layers leveraged the wave heights and wave fluxes in the horizontal directions (x and y) along their nesting boundaries. We utilized the GEBCO 2023 Grid with a resolution of 15 s (~450 m) as the topo-bathymetric input for Layer 1 (GEBCO

Table 4
Numerical model configurations.

Domain	Layer 1	Layer 2	Layer 3	Layer 4
Ymin-Ymax (deg)	2–14	3–6	5.4–5.74	5.52 - 5.62
Xmin-Xmax (deg)	90–100	94–97	95.2–95.45	95.27–95.38
Grid size (m)	1080	216	43.2	10.8
Time step (s)	1.2	0.24	0.048	0.012
Layer ratio	1	5	5	4
Initial condition	Fault Model	Layer-1	Layer-2	Layer-3
Input depth	GEBCO_2023 Grid	BATNAS	BATNAS	Local bathymetry
Input elevation	GEBCO_2023 Grid	BATNAS	BATNAS	DEMs
Friction model	None	None	None	Uniform and 8 LCR
SWE type	Linear	Linear	Linear	Non-linear
Boundary condition	Radiation	Interpolated	Interpolated	Interpolated

Bathymetric Compilation Group, 2023). For Layers 2 and 3 (grid resolutions of 216 m and 43.2 m, respectively), we utilized the Indonesian National Bathymetric Chart (BATNAS) with a resolution of 6 s (~180 m) (tanahair.indonesia.go.id). All topo-bathymetric inputs were resampled to match the resolution of each numerical layer.

The topo-bathymetric input data for the innermost domain (Layer 4) incorporated the depth information from local bathymetric measurements and elevation data from the investigated DEMs. To generate seamless topo-bathymetric datasets with 10 m resolution, we performed the distance-based sampling approach with a 10-m grid interval. We utilized multiresolution water masks, obtained from generated land cover maps, to distinguish between land and water areas. These high-resolution water masks can identify the small water bodies (e.g., ponds and small rivers) that may not be reflected by the local bathymetric data (Fig. S7). To address this, we assigned a uniform depth of −0.5 m to the missing water bodies within the water masks. In total, we created 44 topo-bathymetric input for layer 4, incorporating 11 investigated DEMs and four land cover maps from two distinct periods: 2004 and 2014.

We applied the linear SWE scheme for Layer 1 to 3. For Layer 4, we used the non-linear SWE and incorporated the LCR models as the surface friction components. In addition to LCR models, we included uniform Manning frinction (Manning's n = 0.025) as another friction model in Layer 4. Overall, we simulated 99 inundation scenarios (i.e., 11 DEMs, 8 LCRs, and one uniform Manning model), each with a 2-h running time. All computational topo-bathymetric grids were automatically updated at the start of each simulation to reflect changes in seafloor and land deformation. We leveraged simulation results from Layer 4 to develop the inundation maps at a resolution of 10 m (Tonini et al., 2021).

2.4. Reliability of inundation models: the three sequential assessments

To evaluate the performance of the inundation models, we used reliability criteria based on three sequential assessments, incorporating satellite observations, post-tsunami measurements, and the confidence level associated with inherent DEM error characteristics. First, we compared the models' predictions with observed inundation extents. We set a threshold of 25% difference as a benchmark for acceptable model performance, accounting for the inherent challenges to accurately reproduce the historical tsunami inundation due to data limitations and constraints in the tsunami source model (Sugawara, 2021).

The inundation models meeting the first reliability criteria were further evaluated using the second assessment, focusing on the accuracy of simulated flow depth estimates. The agreement between the simulated and measured flow depths was widely evaluated using Pearson correlation coefficients (r), with coefficient between 0.5 and 1 indicating a strong relationships with measured data (Giblin and Damlamian, 2022). However, Pearson's r correlation had several limitations and cannot evaluate the model's accuracy (Li, 2017). Therefore, we included RMSE as error statistic to select the best-fit models.

Additionally, the uncertainties in mapping coastal inundation are influenced by DEM error characteristics (Hinkel et al., 2021). Therefore, we implemented a third assessment to evaluate the confidence level of inundation maps, incorporating the DEM error characteristics and simulated inundation depths. By assuming that the DEM errors were unbiassed (ME = 0), Gesch (2018) expressed the relationship between DEM errors, inundation depths, and confidence level as:

$$MIH_{68\%} = RMSE\ x\ 2 \tag{1}$$

$$MIH_{95\%} = (RMSE\ x\ 1.96) x\ 2 \tag{2}$$

where MIH is the median of maximum inundation height at land areas (ground elevation >0 m), RMSE is the root mean square error the used DEMs, $MIH_{68\%}$ and $MIH_{95\%}$ are the minimum MIH values required to achieve 68% and 95% confidence level, respectively. Dusseau et al. (2023) suggested that inundation maps should have at least a 68% confidence level to be considered reliable for coastal flood exposure assessment. For example, an inundation model employing an elevation dataset with an RMSE of 2 m can produce a reliable inundation map if the MIH value is at least twice that error value (4m), with smaller MIH values yield a lower confidence level. A simple spreadsheet formula to compute the confidence level is provided in the Supplementary File.

2.5. Tsunami exposure assessment

The inundation maps from models that met all reliability criteria were chosen for the exposure assessment. We superimposed the inundation extent from these maps with built-up and population layers to estimate the areas and populations at tsunami risk. To ensure consistency in the exposure assessment, we matched each inundation map with exposure variables that were derived from the same land cover information. For example, inundation maps resulting from models using friction parameters of LCR04-30 were overlaid with exposure layers of BU04-30 and POP04-30. We then analyzed how differences in DEMs, roughness parametrization, exposure datasets, and land cover evolution influenced the exposure estimates. To understand the potential biases when using different hazard information, we also compared the exposure estimates based on the simulated inundation maps against the estimation from the satellite-observed inundation limit of the 2004 IOT.

3. Results

3.1. Geolocation and radiometric consistency

The geolocation offsets across the satellite images ranged from a minimum of 10 m (observed in SPOT 5 2014) to a maximum of 55

m (observed in SPOT 5 2004). The co-registration process effectively reduced geolocation misalignment by 85.6%–92.2%. Meanwhile, the NDVI comparisons showed that radiometric inconsistencies, measured in root mean square error (RMSE), ranged from 0.26 to 0.33. The spectral normalization reduced the error to a range of 0.02–0.04, improving radiometric consistency by 87.5%–92.3%. Figs. S8 and S9 of the Supplementary File show details of spatial and spectral consistencies, respectively.

3.2. Land cover classification and LCR models

Fig. 3 presents the land cover classification results, covering the innermost domain of the numerical model (Layer 4). For 2004, the accuracy of land cover maps increased with finer image resolutions, with an overall accuracy and a Kappa index of 83.8% and 0.73 for 30 m (LC04-30), 93.4% and 0.89 for 10 m (LC04-10), and 95.2% and 0.92 for 5 m (LC04-5). Meanwhile, the 2014 land cover map (LC14-5; Fig. 3d) achieved an overall accuracy of 92.7%, with Kappa index of 0.88. All land cover maps demonstrated a low accuracy for the bare class, with an average F1 score of 0.7. The highest F1 score with an average of 0.97 was observed in the water class, followed by the built-up class with an average F1 score of 0.94. Table S7 in the Supplementary File provides details of the confusion matrices and accuracy assessment.

We observed that image resolution and temporal evolution influenced the class-area estimates (Table S8). A detailed analysis of the interrelationship between spatiotemporal evolution and land cover classification was presented in Section 3.3. Variations in class-area estimates affected the calculated density of built-up areas. Built-up areas from LC04-30 were dominated by high-density (52.46%),

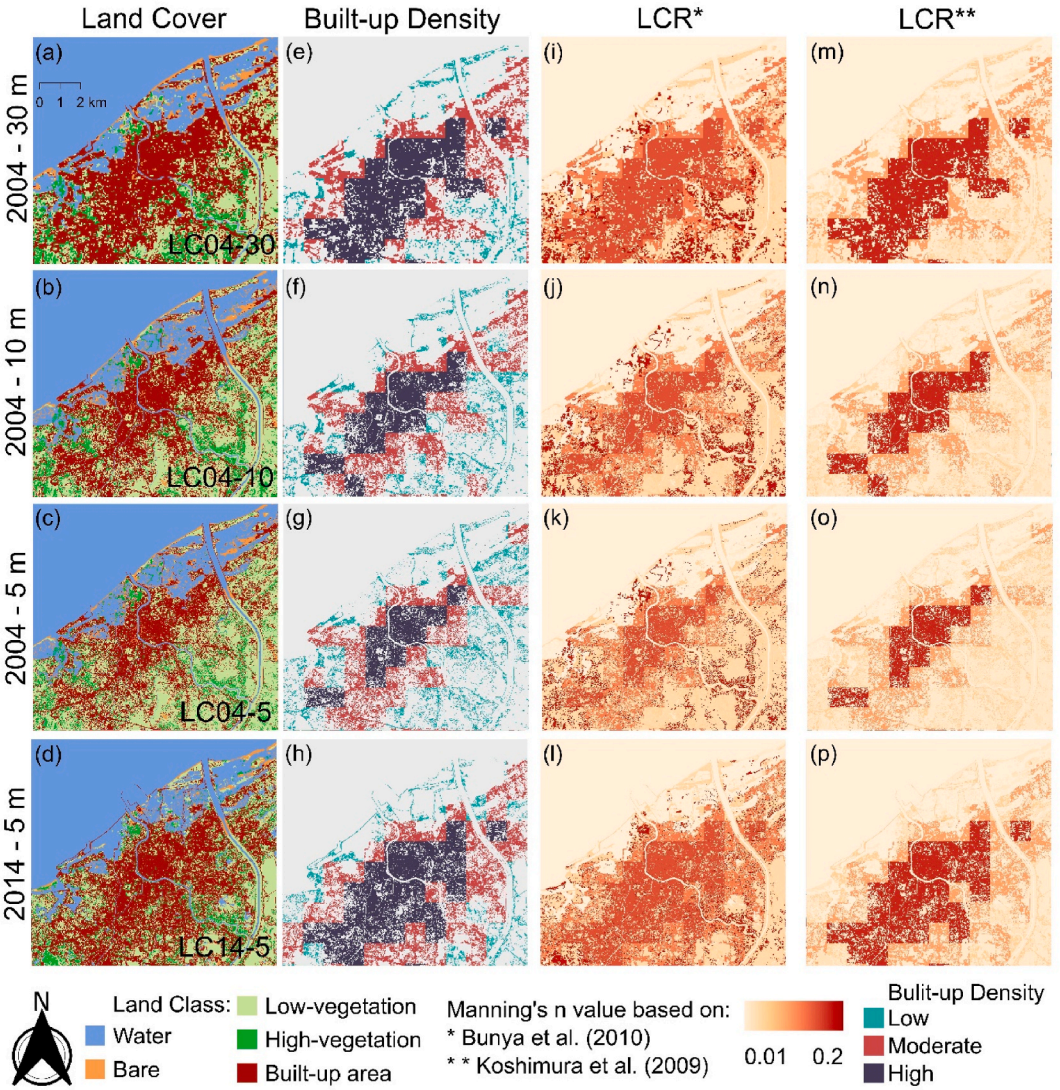

Fig. 3. SDED outputs at various spatial and temporal resolutions: (a–d) Land cover maps, (e–h) Built-up areas density estimates, and (i–p) Land cover roughness (LCR) models.

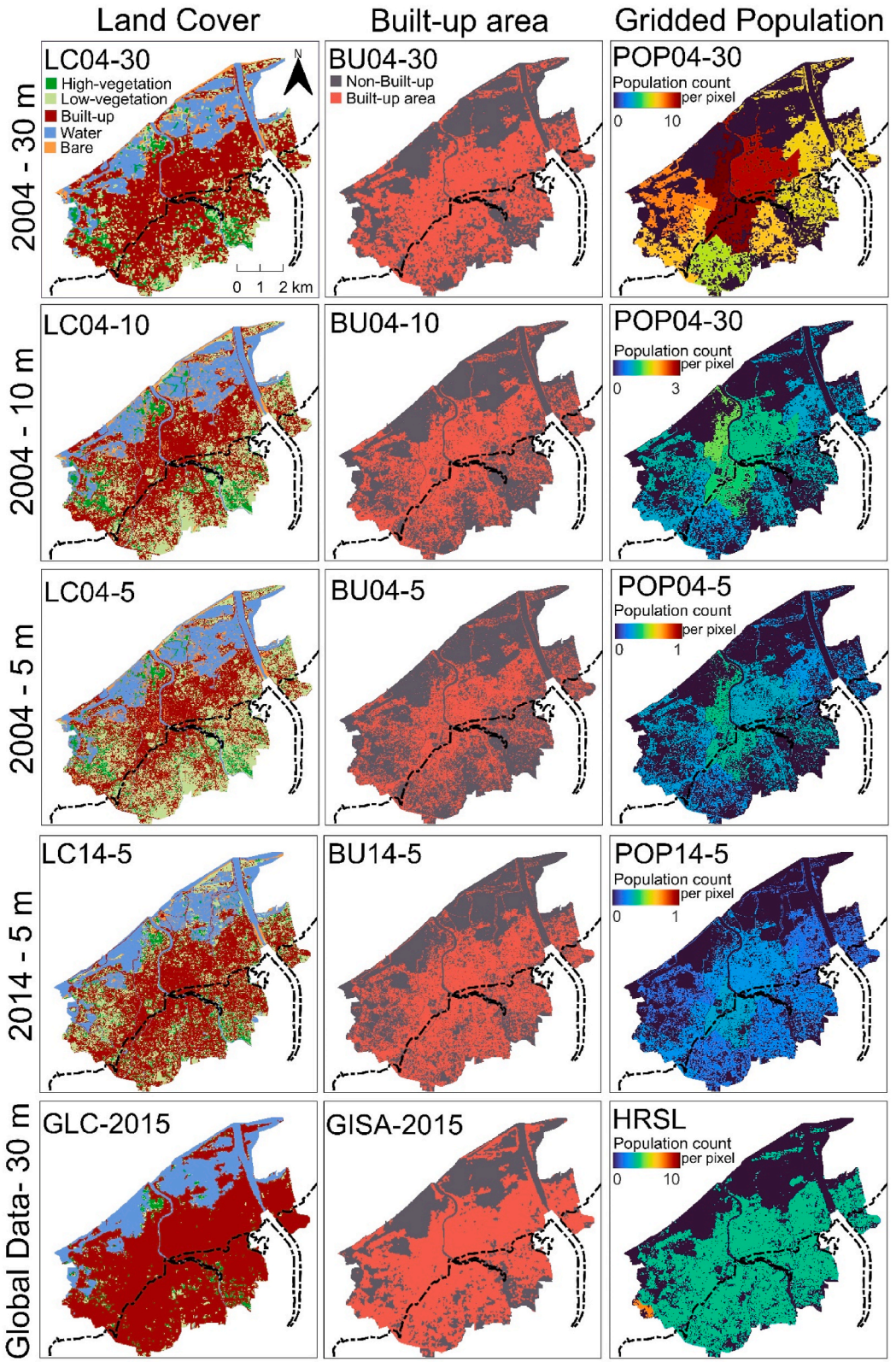

Fig. 4. The exposure datasets within Banda Aceh region: land cover maps, built-up areas and gridded populations. The black dashed line indicates the 2004 IOT inundation limit.

followed by moderate-density at 34.47%, and low-density areas at 12.96% (Fig. 3e). In contrast, moderate-density built-up areas were predominant in both LC04-10 and LC04-5.

Both LC04-10 and LC04-5 showed a distinct pattern in their minimal proportion. LC04-10 demonstrated the lowest proportion in low-density built-up areas (Fig. 3f), whereas LC04-5 had minimal proportion in high-density built-up areas (Fig. 3g). For LC14-5, approximately 11.67% of built-up areas were classified as low-density, followed by moderate at 37.02% and high-density at 51.31% (Fig. 3h). By using information from these land cover maps and built-up density estimates, we generated multiresolution land cover roughness (LCR) models for the epoch of 2004 and 2014, as shown in Fig. 3i–p.

3.3. Exposure datasets and change analysis

Fig. 4 presents the land cover maps, built-up areas, and gridded population datasets within Banda Aceh region. Estimated areas of the low-vegetation class showed a clear upward trend with increasing map resolution (LC04-30: 972.99 ha, LC04-10: 1391.4 ha, and LC04-5: 1750 ha). In contrast, we observed a downward trend for the built-up class with estimated areas of approximately 3219.5 ha for LC04-30, 2647.31 ha for LC04-10, and 2288.61 ha for LC04-5. This contrasting trend suggests that a land cover map with lower resolutions is more likely to misclassify low-vegetation as built-up pixels. The temporal comparison of land cover maps with a similar resolution (i.e., LC04-5 vs. LC14-5) revealed a decrease in all land cover classes by 2014, except for built-up areas. Low-vegetation areas had reduced by 8% (63.36 ha) within the 2004 IOT inundation extent and by 33% (581.19 ha) across the entire Banda Aceh region. The overall reduction reached a significant of 796.50 ha when comparing temporal land cover maps with coarser resolution (i.e., GLC-2015 vs. LC04-30). This was because GLC-2015 predicted larger built-up areas (4110 ha) that covered nearly 70% of the land cover, compared to only 51% (3007.76 ha) by LC14-5. As a result, GLC-2015 underestimated the low-vegetation class.

In contrast to low-vegetation, built-up areas expanded to 3007.76 ha by 2014, increasing by 719.15 ha compared to 2004 (BU14-5 vs. BU04-5). Leveraging information from the 2004 IOT inundation limit, we divided Banda Aceh region into affected (within the inundation extent) and non-affected zones (outside the inundation extent). For 2004, more than 60% of the total built-up areas were concentrated within the affected zone, with coarser resolution datasets resulting in larger estimates of affected areas. By 2014, both the 30 m GISA-2015 and BU14-5 showed that the built-up area distribution remained largely located within the affected zone, with GISA-2015 produced larger estimates of affected built-up areas than BU14-5 (i.e., GISA-2015: 2375.91 ha, BU14-5: 1746.05 ha). Additionally, the temporal comparisons at 30 m (BU04-30 vs. GISA-2015) and 5 m resolution (BU04-5 vs. BU14-5) revealed a distinct pattern in the built-up area evolution. The coarser dataset comparisons suggested that 61% of the increase (508.07 ha total) was located within the affected zone. In contrast, a comparison of finer datasets suggested that 71% of built-up area expansion (719.15 ha total) was concentrated outside the affected zone. These findings reveal that differences in spatial resolution may lead to contrasting interpretations of risk evolution.

Meanwhile, population estimates per pixel varied across different resolutions, with population counts per hectare ranging from 60 to 130 for POP04-30, 80–140 for POP04-10, and 100–140 for POP04-5. The gridded population datasets suggested that more than 65% of total Banda Aceh population in 2004 lived within the 2004 IOT inundation extent, with finer datasets estimating more than 500 additional people (POP04-30: 174,554, POP04-10: 175,321, and POP04-5: 176,003). POP14-5 showed that population distribution by 2014 remained predominantly concentrated within the affected zone. However, the population living within the affected zone declined to 144,525, decreasing by more than 30,000 people compared to POP04-5.

Population decline was also observed when comparing population datasets of 30 m resolution (HRSL vs. POP04-30), showing a decrease of 100,100 people. The significant difference aligns with the total Banda Aceh population estimate projected by HRSL, which was approximately half that of POP14-5 and local census data (i.e., POP14-5: 249,500, HRSL: 129,367). The decreasing population trend contrasted with the expansion of built-up areas, suggesting that built-up expansion in the affected zone does not correlate linearly with population growth. Detailed calculations of population, built-up areas, and land cover class estimates are provided in Tables S9–S11 of the Supplementary File.

Table 5
Error metrics of DEMs in the low elevation coastal zone.

Metric (m):	RMSE			ME			MAE		
DEM [Resolution]	*AVG*	*BU*	*HV*	*AVG*	*BU*	*HV*	*AVG*	*BU*	*HV*
AW3D30 [30 m]	3.13	4.12	4.27	1.66	3.43	3.54	2.54	3.46	3.63
COP30 [30 m]	1.64	2.11	2.85	0.37	1.41	1.83	0.94	1.63	1.97
CRAWDEM [30 m]	2.06	2.39	3.14	0.83	1.73	2.16	1.26	1.90	2.29
CoastalDEM [90 m]	**1.53**	**1.27**	**1.40**	−0.98	**−0.34**	**−0.73**	1.30	**1.00**	**1.07**
DEMNAS [8 m]	2.35	1.94	3.16	**−0.32**	0.72	2.12	1.78	1.40	2.42
DiluviumDEM [30 m]	**1.18**	**1.02**	**1.25**	−0.36	**−0.21**	**0.10**	0.70	**0.71**	**0.81**
EDEM [30 m]	1.78	1.97	3.00	0.48	1.30	2.02	1.01	1.53	2.19
FABDEM [30 m]	**1.09**	**1.11**	**1.38**	**0.02**	**0.43**	**0.65**	**0.59**	**0.81**	**0.97**
MERIT [90 m]	2.74	3.30	3.57	1.58	2.80	3.00	2.29	2.86	3.13
NASADEM [30 m]	2.14	2.49	3.70	**0.07**	1.20	2.31	1.60	1.91	2.73
SRTM [30 m]	3.13	3.87	5.21	1.56	3.06	4.25	2.45	3.17	4.32

AVG: Average errors. All land cover classes, except water; **BU**: built-up area; **HV**: High-vegetation.

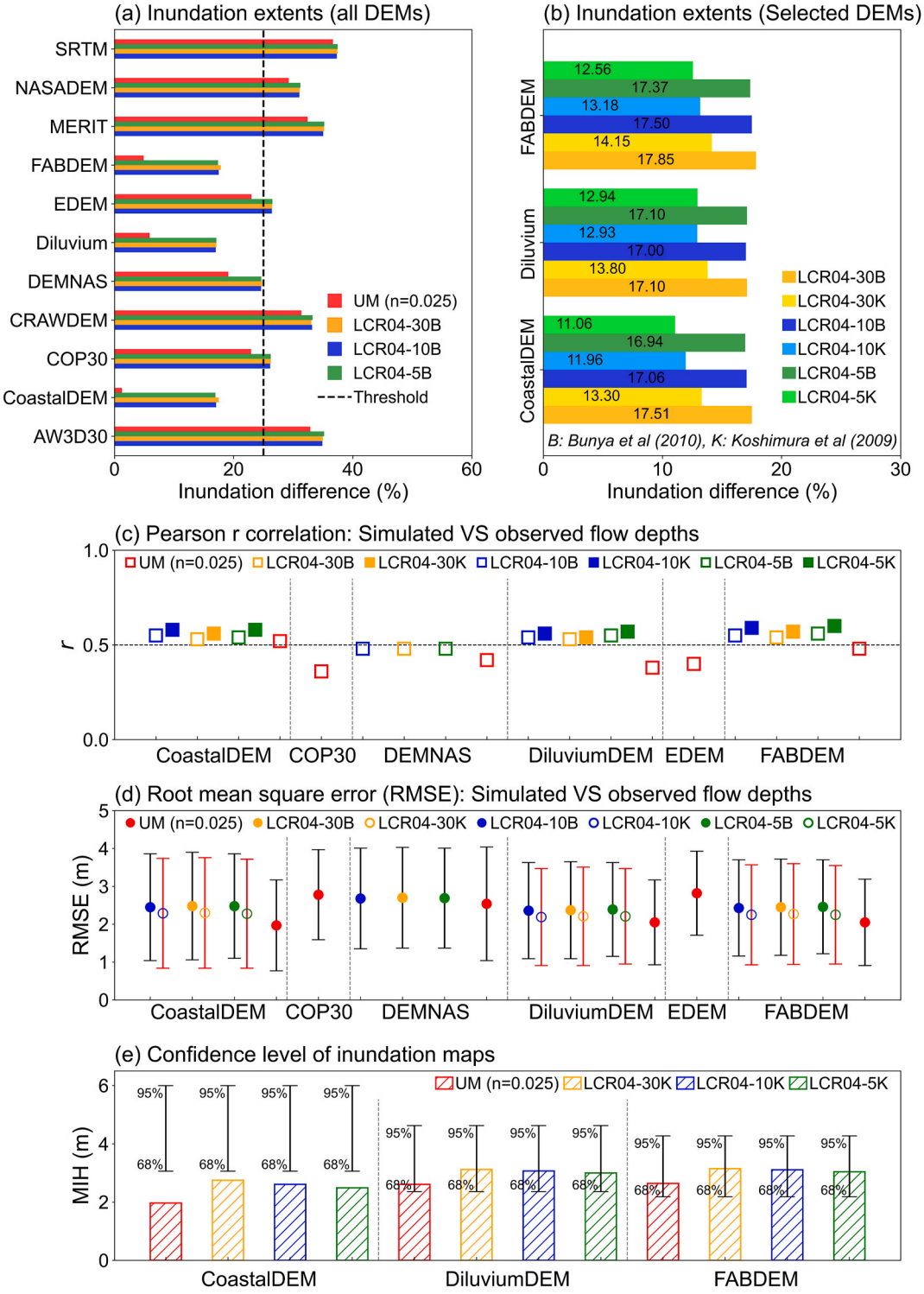

Fig. 5. Simulated vs. observed inundation extents (first criteria): (a) All DEMs, with LCR models based on Bunya et al. (2010); (b) Selected DEMs, with LCR models based on different Manning sources. Simulated vs. observed flow depths (second criteria): (c) Pearson R correlation; (d) RMSE. Third criteria: (e) Confidence level of inundation maps, LCR models based on Koshimura et al. (2009).

3.4. DEM's statistical error metrics

Table 5 summarizes the error metrics for each DEM at elevations below 10 m across the different land cover types. We used approximately 460,000 ICESat-2 ground elevation points to compute the RMSE, MAE, and ME. Overall, the accuracy of the error-reduced DEMs consistently outperformed the original DEMs, except for CRAWDEM. This is likely due to the absence of a full calibration process for newly added data (Lachaise and Schweißhelm, 2023), leading to EDEM maintaining better accuracy out of nine individual comparisons.

The improved variants of COP30 (FABDEM and DiluviumDEM) consistently exhibited more accurate RMSE and MAE values than the other DEM datasets. On average, FABDEM performed slightly better than DiluviumDEM, with elevation errors almost normally distributed (ME = 2 cm). However, when focusing on specific land cover types, DiluviumDEM outperformed FABDEM with an RMSE of 1.02 m for built-up and 1.25 m for highly vegetated areas. For the improved SRTM variants, CoastalDEM outperformed MERIT and NASADEM, particularly within built-up (RMSE: 1.27 m and MAE: 1 m) and highly vegetated regions (RMSE: 1.4 m and MAE: 1.07 m). However, CoastalDEM showed significant negative biases with an average of 1 m, underestimating the elevation of coastal low-lying areas compared to the ground truth data.

Interestingly, the average accuracy of the 8 m resolution local DEMNAS was lower than some global DEMs with coarser resolution, including FABDEM, DiluviumDEM, CoastalDEM, COP30, and NASADEM. However, DEMNAS outperformed MERIT across different land cover types and showed better accuracy than COP30 and NASADEM in built-up areas. The results indicated that MERIT was the least accurate dataset among the error-reduced DEMs, overestimating elevation, with ME reaching 1.58 m. Similarly, its original datasets, AW3D30 and SRTM, showed the highest overestimation compared with EDEM and COP30. Specifically, the positive errors of SRTM and AW3D30 in built-up areas reached 3.87 m and 4.12 m, respectively. For SRTM, these errors increased significantly by 5 m in highly vegetated regions.

3.5. Reliability of inundation models

Fig. 5 presents the results of three sequential validation assessments for inundation models. Overall, models underestimated the actual inundation extent of the 2004 IOT. Inundation models with a uniform Manning coefficient (UM) resulted in better agreement with satellite observations, compared to those using LCR models based on Bunya et al. (2010) coefficients (Fig. 5a). The best agreement was observed when UM model was paired with CoastalDEM. Given the first reliability rule (i.e., simulated and observed inundation extents differed by less than 25%), three error-reduce DEMs (CoastalDEM, DiluviumDEM, and FABDEM), and the local DEMNAS satisfied the threshold when paired with both UM and LCR models. Meanwhile, COP30 and EDEM could meet the given threshold when combined with UM, but not with LCR models. In contrast, inundation models using elevation data of SRTM, AW3D30, CRAWDEM, MERIT, and NADADEM did not satisfy the first reliability assessment.

To understand the uncertainty introduced by different Manning coefficients sources, Fig. 5b shows the differences in inundation extents between LCR models using coefficients from Bunya et al. (2010) and Koshimura et al. (2009). Notably, combinations of error-reduced DEMs with variable Manning coefficients from Koshimura et al. (2009) produced a closer match to the satellite observations. This could be attributed to Manning coefficient for vegetated areas in Koshimura et al. (2009) was lower than in Bunya et al. (2010), which eventually led to larger inundation extents. Furthermore, the relationship between inundation extents, DEMs, and resolution of LCR models varied by coefficient sources. Using Koshimura et al. (2009) coefficients, CoastalDEM produced larger inundation than Diluvium and FABDEM. In contrast, DiluviumDEM would exhibit greater inundation than the other two DEMs if Manning coefficients were derived from Bunya et al. (2010), particularly for LCR models with 10 and 30 m resolution. Although the differences were minimal, we observed that finer resolution LCR models using any Manning sources consistently yielded larger inundation extents, especially when paired with CoastalDEM and FABDEM.

The second reliability assessment showed that UM model produced flow depths with lower correlation with observed data, with models using DEMNAS, EDEM, DiluviumDEM, and COP30 had Pearson's r coefficients being less than 0.5 (Fig. 5c). However, the UM model consistently produced more accurate flow depth estimates than LCR models, with RMSE of 1.97 m for CoastalDEM, 2.05 m for FABDEM, and 2.06 m for DiluviumDEM (Fig. 5d). Similar to inundation extents, we observed that LCR models based on Koshimura et al. (2009) coefficients resulted in more accurate flow depth, with finer resolution models yielding lower RMSE estimates. Detailed comparisons of simulated and observed flow depths are presented in Figs. S10 and S11. We selected models with RMSE lower than 2.5 m to be further evaluated using the third reliability assessment. Given this, models using DEMNAS, EDEM, and COP30 did not meet the required threshold. Additionally, among the LCR models we only selected the Koshimura et al. (2009) coefficients since they predicted more accurate flow depths.

For the third reliability assessment, we computed the confidence levels of selected inundation models based on their MIH estimates and DEM error characteristics. For MIH calculations, we excluded all flow depth estimates from water bodies (DEMs <0 m). The assessment showed that models using CoastalDEM failed to achieve the minimum confidence level of 68% (Fig. 5e). In contrast, FABDEM and Diluvium exceeded the minimum confidence levels, with UM produced lower confidence level compared to LCR models. FABDEM consistently outperformed DiluviumDEM, with confidence levels of 85.1% vs. 81.4% for LCR04-30, 84.7% vs. 80.7% for LCR04-10, and 84.7% vs. 80.7% for LCR04-5. This can be attributed to larger MIH estimates produced by FABDEM and its lower elevation error (RMSE – FABDEM: 1.09 m; DiluviumDEM: 1.18 m). We observed a different trend between total and overland inundation (excluding water bodies). While CoastalDEM consistently produced larger total inundation, inundation maps demonstrated that it has smaller overland inundated areas than the two other DEMs (Fig. 6).

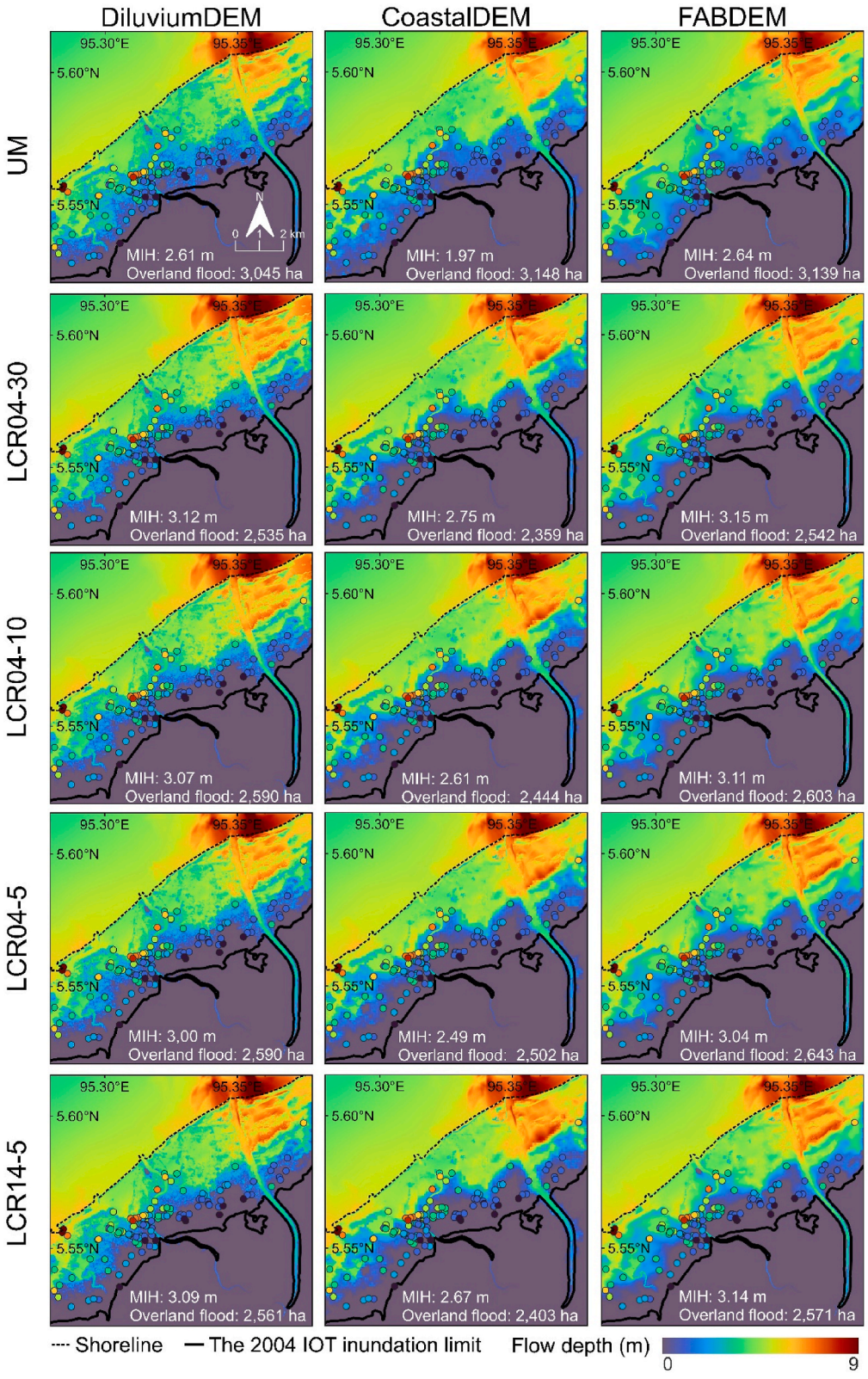

Fig. 6. Distribution of maximum flow depths, with MIH is the median values. Overland flood indicates inundation areas outside water bodies, while coloured markers represent the observed flow depths.

3.6. Tsunami exposure assessments

Given the reliability assessment, we have eight inundation models that satisfied all given thresholds. These models were combinations of FABDEM and DiluviumDEM with UM and the 2004 LCR models. However, for the tsunami exposure assessments, we focused on scenarios using the LCR models. To understand the effects of land cover change, we included the inundation models using the 2014 LCR model (LCR14-5). Fig. 7 presents the exposure estimates for Banda Aceh region, derived by superimposing the simulated and satellite-observed inundation with built-up and gridded population datasets. Results showed that satellite observation consistently projected twice the exposure estimates provided by the simulations. This could be attributed to the smaller inundation extents obtained by simulations. Similar to satellite observations, simulations showed a proportional relationship between exposed and total estimates of built-up areas and population.

Despite having lower overland inundation than FABDEM, we observed that DiluviumDEM projected higher exposure estimates (Fig. 7c), with exposed built-up areas ranging from 736 ha (BU04-5) to 970 ha (BU04-30). Consequently, DiluviumDEM projected higher exposed population estimates, with an average of 5000 more people than those projected by FABDEM (Fig. 7d). By 2014, DiluviumDEM predicted a slightly larger increase in exposed areas by 52.2 ha, compared to only 51.1 ha by FABDEM. This increase followed by DiluviumDEM predicted 3869 more people exposed to tsunami. This difference likely reflects variations in inundation distribution, with DiluviumDEM potentially inundating more built-up areas than FABDEM.

4. Discussion

4.1. Error-reduced DEMs, LCR model resolutions and inundation extents

Given the results, the improved variants of global DEMs have fewer inherent errors in coastal low-lying areas compared to their

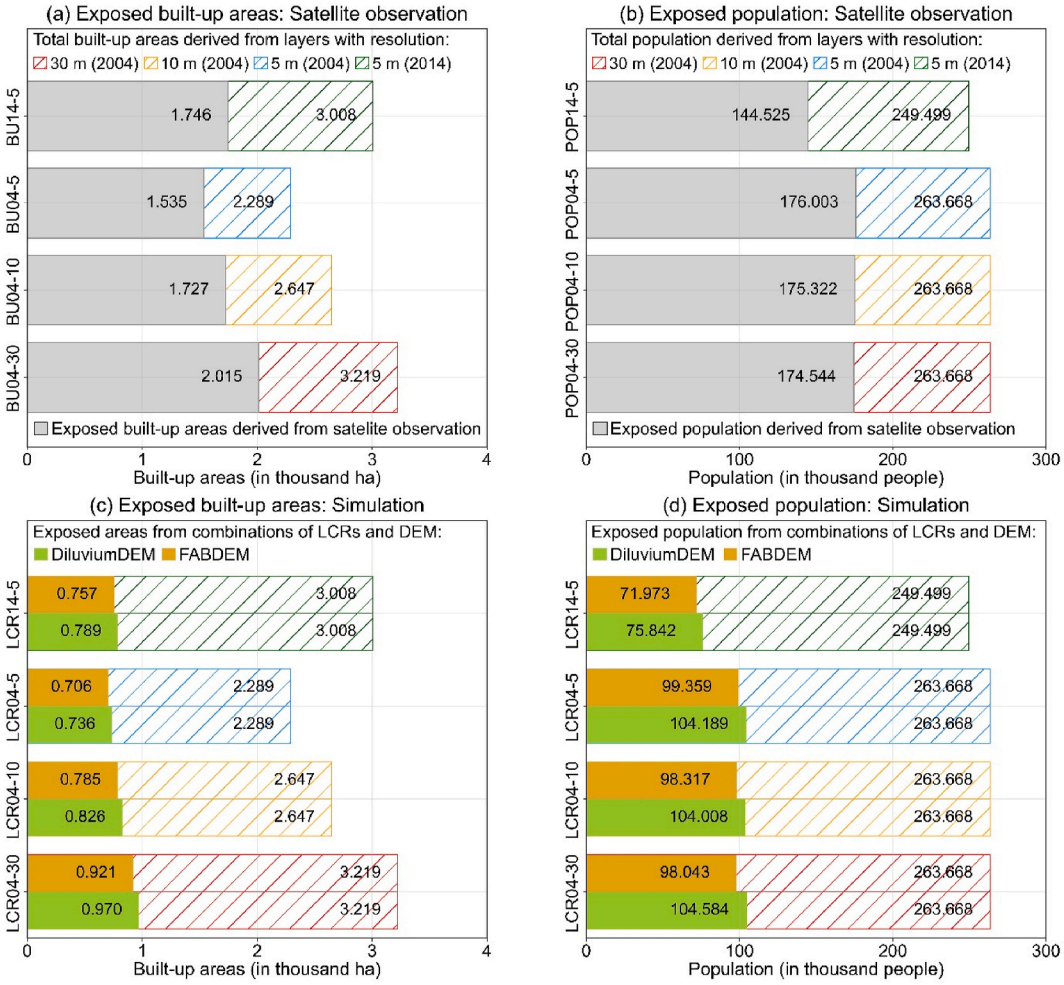

Fig. 7. Exposure estimates using hazard information of: (a–b) Satellite observation, (c–d) Simulations.

original datasets. Some of these DEMs, with spatial resolutions ranging from 30 m to 90 m outperformed the 8m resolution local DEMNAS. This highlights that spatial resolution should not be used as a sole indicator to define DEM performance, as it is influenced by various factors, including generation techniques and geographical settings (Liu et al., 2021; Hawker et al., 2018). Despite having better accuracy, inundation models using error-reduced DEMs still underestimates the actual inundation extent of the 2004 IOT.

The underestimations likely correlate with several factors, such as the acquisition period of these DEMs (e.g., most data were collected between 2006 and 2020) and limitations on the onshore bathymetric data used. As highlighted by Sugawara (2021), the evolution of coastal morphology and land cover change after a tsunami disaster might present a significant challenge for accurately reconstructing the historical tsunami estimates. The underestimation may also correlate with the accuracy of the tsunami source model. It should be noted that the simulated inundations are constrained to the Mw 9.2 fault inversion model from Koshimura et al. (2009). Using alternative tsunami source models to reproduce the 2004 IOT inundation in Banda Aceh region, such as the one proposed by Yanagisawa et al. (2010), may yield different simulation results, potentially leading to a different agreement with the actual inundation.

The inundation assessment showed that CoastalDEM coupled with UM model resulted in the largest inundation extent. Although this showed the best agreement with the observed inundation extent, the result is most likely attributed to CoastalDEM having a larger negative bias than FABDEM and DiluviumDEM, with an average of −1 m. This large negative bias can underestimate the ground elevation, eventually leading to inundation overestimation (Liu et al., 2021). It should be highlighted that all our inundation models consistently underestimated the actual inundation. Given this, the bias in elevation data likely improved the agreement with observed data, although this only reflects our specific situation. Interestingly, when paired with LCR models using Manning coefficients proposed by Bunya et al. (2010) at 10 m and 30 m resolution, CoastalDEM resulted in lower inundation extents than DiluviumDEM. In contrast, when DiluviumDEM was paired with LCR model at 5 m resolution using coefficients from Koshimura et al. (2009), it was outperformed by FABDEM, despite having a larger negative bias (FABDEM: +0.02 m; DiluviumDEM: −0.36 m). These findings suggest that the interaction between inundation and the parameterization of surface friction is unique to each DEM.

Inundation maps showed that CoastalDEM had less overland inundation than FABDEM and DiluviumDEM. This results from CoastalDEM having more water pixels than the two other DEMs. However, when paired with finer-resolution LCR models, CoastalDEM tended to produce larger overland inundation. This was also demonstrated by FABDEM. Increasing the LCR resolution from 30 m to 5 m subsequently increased the inundated areas by 6% for CoastalDEM and 4% for FABDEM. Additionally, both DEMs uniformly showed a decrease in overland inundation by 2014, suggesting that the land cover change influenced the inundation behaviour. However, a contrasting pattern emerged: models with larger inundation extents tended to have smaller MIH values.

This contrasting pattern may be caused by several interrelated factors. For example, the flat terrain characteristics of Banda Aceh may lead to a wider extent of inundation (Devitt et al., 2023). On the other hand, the expansion of built-up areas likely increases flow resistance, reduced flow infiltration capacity, and leads to smaller inundation coverage (Koyama and Yamada, 2022). Moreover, finer-resolution LCR models enable a better representation of drainage systems (i.e., small rivers and ponds), which can influence the simulated flow depth. This is consistent with our inundation model setting, where we incorporated small water bodies by adjusting the topo-bathymetric inputs based on the chosen land cover maps.

The reliability assessment identified that combination of FABDEM and DiluviumDEM with any roughness models met all reliability criteria. Given the elevation error analysis, these two DEMs consistently exhibit lower errors, particularly within the built-up areas. This suggests that elevation error distributions within built-up areas might be a valuable indicator in selecting global DEMs for inundation modeling, especially in locations dominated by this land cover type. Additionally, error distributions revealed that DiluviumDEM had more negative errors than FABDEM within built-up areas (Fig. S12 of the Supplementary File). This might explain variations in inundation distribution where DiluviumDEM inundated more built-up areas than FABDEM. While the error distribution also showed that CoastalDEM exhibited good elevation accuracy in built-up areas (RMSE: 1.27 m), it demonstrated low confidence levels. This lower confidence level might be attributed to its high negative bias within built-up areas.

4.2. *Hazard information and exposure datasets*

The exposure estimates were proportional to the extent of inundation. This is evident from satellite observations, which captured larger inundation extents and subsequently projected twice those estimated by numerical simulations. Additionally, the characteristics of exposure data have a critical role in impact assessment. We observed that finer-resolution built-up datasets tend to exhibit a lower exposure estimate, while finer-resolution gridded populations result in a higher estimate of population exposed to tsunami.

Both simulations and satellite observations estimated an increase in exposed urban areas in 2014. This is consistent with the built-up expansion trend in Banda Aceh. Notably, ensuring consistency in exposure data resolution is critical in assessing the exposure evolution. For example, comparing the exposure estimates from coarser built-up layers (e.g., 2004: BU04-30 or BU04-10) with finer datasets (e.g., 2014: BU14-5) can lead to a decreasing trend, potentially leading to misinterpretation of the risk evolution. Even with a similar resolution, bias in exposure assessment persists when exposure layers are developed from different methodologies. For example, satellite observations detected that the population residing within the 2004 IOT inundation extent declined by more than 30,000 people by 2014. This was obtained by comparing the gridded population datasets at 5 m resolution (i.e., POP04-5 vs. POP14-5). However, the population decline increased three times higher (more than 100,000 people) when the resolution of gridded population data was at 30 m (HRSL vs. POP04-30).

This discrepancy arises from differences in the spatial disaggregation levels and input data. In detail, our gridded population layers incorporated the 2014 local census data of Banda Aceh at subdistrict level, while the global HRLS disaggregated population estimates from the Gridded Population of the World collection version 4 (GPWv4) at the municipality or district level (Tiecke et al., 2017). These

findings emphasize the importance of understanding the properties of global exposure data and carefully choosing the best available data that fits specific utilization purposes. Doing so can minimize the incompatibility that can lead to inaccurate projection of exposure evolution, as highlighted by Bernhofen et al. (2022).

4.3. Limitations in reliability criteria and exposure estimates

While the results of this study can provide valuable insight for the sensitivity of tsunami models to input datasets, it should be noted that certain limitations still exist. First, the evaluation of DEMs and surface roughness parameterizations is highly sensitive to the established threshold. For example, given the agreement between the simulated and satellite-derived inundations, increasing the threshold from 25% to 10% could suggest that the application of LCR models results in unreliable inundation estimates. Likewise, reducing the threshold by 10% would make SRTM and AW3D30 classified "reliable" despite their error characteristics. Second, while resulting in less accurate prediction of inundation depths, the use of UM model has better agreement with the observed inundation extent than LCRs. This suggests that the application of UM could still be reliable to some extent. It is also crucial to highlight that uncertainties in reliability assessment may persist because of inaccurate records of tsunami measurements and potential geolocation offsets between simulated and measured flow depth points.

Third, the reported results are constrained to a specific tsunami source model and the flat coastal plain characteristics of our research location. These factors must be considered when comparing the reported results to other locations with different topographic settings or hazard models. For example, given its inherent elevation errors within the Banda Aceh region, CoastalDEM would achieve the required confidence level when the simulated MIH was 3.06 m at minimum (RMSE: 1.53 m). However, the obtained MIH values were lower, resulting in confidence levels of only 48% (UM), 63.2% (LCR04-30), 60.6% (LCR04-10), and 58.3% (LCR04-5), respectively. Variations in tsunami scenarios and terrain characteristics can lead to different MIH and elevation error estimates, which will alter the computed confidence levels of CoastalDEM. Thus, our results should not be used to provide an absolute indication of the accuracy of different input data choices, but rather, to illuminate how different input data choices can modify the simulated inundation extent.

Fourth, the reported exposure estimates are influenced by built-up area definitions. Bonatz et al. (2024) noted that variation in built-up area definitions can lead to estimate discrepancies of up to 65%. Meanwhile, our gridded population layers may underestimate the settlement-associated properties, including settlement density, number of stories, and type of settlement (e.g., residential, schools, or public buildings). The underestimation may also result from daily mobility patterns, particularly those related to work and school (Lloyd et al., 2019). This mobility potentially results in the unregistered or floating population, increasing the bias from the exposed population estimates (Wu and Zhang, 2021).

The floating population is reflected by local census data, which reported a decline in the population of Banda Aceh by 3000 people, i.e., from 265,111 in 2018 to 261,969 in 2023 (BPS, 2024). In contrast, the same report revealed that number of university students in Banda Aceh was recorded to increase by 27,142, from 51,331 in 2018 to 78,473 in 2023. These contrasting records may explain the nonlinear relationship between the built-up area estimates and the population recorded by 2014. Given its administrative role as the capital city of Aceh Province, Banda Aceh hosts many universities and government offices which could attract people from other districts and provinces (Meilianda et al., 2019). This influx potentially leads to the development of built-up areas (e.g., student apartments), even though the city's population may not be significantly increasing.

4.4. Recommendations for the future research

Given the discussed limitations, we recommend future studies to reproduce other historical tsunami events with multiple source models to evaluate the robustness of the three sequential validation assessments introduced in this study. This could also map the behaviors of error-reduced DEMs and LCR models under different terrain characteristics (e.g., slope and land cover setting). Additionally, future studies should incorporate the elevation dataset of DeltaDTM (Pronk et al., 2024), a new improved variant of COP30, which available after this work is completed.

Considering the heterogeneous behaviors of tsunami source properties, it is necessary to simulate a wide range of hypothetical tsunami scenarios to represent hazard variability (Davies, 2019; Davies and Griffin, 2020). This could illuminate the effectiveness of land cover roughness applications under different tsunami scenarios. For more granular exposure assessments, future studies should employ exposure data at finer spatial scales, such as building or village levels. This would provide a more detailed picture of vulnerable populations. Additionally, investigating the impact of "floating populations" is essential, particularly in areas that experience significant seasonal fluctuations due to tourism, education, or economic activities.

After the 2004 IOT, the reconstruction of Banda Aceh City adopted a land use planning that incorporated historical hazard information into the physical zoning schemes (BAPPENAS, 2005). However, our analysis reveals the concerning trends. By 2014, the majority of Banda Aceh's population remained within areas inundated during the 2004 IOT, and the extent of built-up areas had exceeded the pre-tsunami levels. These findings might indicate that post-tsunami developments might not fully adhere to the master plan, as also observed in many locations post-disaster recovery (Iuchi et al., 2023). To support long-term tsunami risk preparedness in Banda Aceh, future studies should comprehensively investigate the extent of land use deviation along with the underlying reasons that hindered its implementation.

5. Conclusions

The interrelationship between DEM error characteristics, LCR model resolutions, and inundation estimates is unique to each DEM. Incorporating spatially variable roughness Manning coefficients improved inundation depth predictions, with finer resolution LCR models produced better predictions at certain extents. Compared to DEM error characteristics, increasing the resolution of LCR models had a minimal effect on tsunami estimates. Nevertheless, this effect could still be perceptible for exposure assessments, particularly in densely populated urban areas.

CRediT authorship contribution statement

Rajuli Amra: Writing – original draft, Methodology, Investigation, Formal analysis, Conceptualization. **Susumu Araki:** Writing – review & editing, Supervision. **Christian Geiß:** Writing – review & editing, Supervision. **Gareth Davies:** Writing – review & editing, Supervision, Conceptualization.

Submission declaration

This paper has not been published or submitted elsewhere and is not under consideration at another journal. All authors approve the publication of this paper.

Data and code availability

The data and code used in this study are mostly publicly accessible. Links are provided in the Supplementary File. Any remaining data and code will be available upon request.

Ethical statement

I, the Corresponding Author, declare that this manuscript is original, has not been published and is not under consideration by another journal. All authors have no conflicts of interest and have agreed to submit this manuscript to this journal.

I confirm that the manuscript has been read and approved by all named authors and that there are no other persons who satisfied the criteria for authorship but are not listed. I further confirm that the order of authors listed in the manuscript has been approved by all of us.

Declaration of competing interest

The authors declare that they have no known competing financial interests or personal relationships that could have appeared to influence the work reported in this paper.

Acknowledgments

We acknowledge Dr. Xioaming Wang of GNS Science, New Zealand for providing COMCOT post-processing MATLAB codes. Additionally, we thank Dr. Syamsidik of Tsunami Disaster and Mitigation Research Center (TDMRC), Indonesia for providing the local bathymetry data. GD publishes with the permission of the CEO, Geoscience Australia.

Appendix A. Supplementary data

Supplementary data to this article can be found online at https://doi.org/10.1016/j.rsase.2024.101438.

Data availability

Data will be made available on request.

References

BAPPENAS, 2005. Master Plan for the Rehabilitation and Reconstruction of the Regions and Communities of the Province of Nanggroe Aceh and the Islands of Nias, Province of North Sumatera. Jakarta, Indonesia.

Behrens, J., Løvholt, F., Jalayer, F., Lorito, S., Salgado-Gálvez, M.A., Sørensen, M., Abadie, S., Aguirre-Ayerbe, I., Aniel-Quiroga, I., Babeyko, A., Baiguera, M., Basili, R., Belliazzi, S., Grezio, A., Johnson, K., Murphy, S., Paris, R., Rafliana, I., De Risi, R., Rossetto, T., Selva, J., Taroni, M., Del Zoppo, M., Armigliato, A., Bureš, V., Cech, P., Cecioni, C., Christodoulides, P., Davies, G., Dias, F., Bayraktar, H.B., González, M., Gritsevich, M., Guillas, S., Harbitz, C.B., Kânoğlu, U., Macías, J., Papadopoulos, G.A., Polet, J., Romano, F., Salamon, A., Scala, A., Stepinac, M., Tappin, D.R., Thio, H.K., Tonini, R., Triantafyllou, I., Ulrich, T.,

Varini, E., Volpe, M., Vyhmeister, E., 2021. Probabilistic tsunami hazard and risk analysis: a review of research gaps. Front. Earth Sci. 9, 628772. https://doi.org/10.3389/feart.2021.628772.
Bernhofen, M.V., Cooper, S., Trigg, M., Mdee, A., Carr, A., Bhave, A., Solano-Correa, Y.T., Pencue-Fierro, E.L., Teferi, E., Haile, A.T., Yusop, Z., Alias, N.E., Sa'adi, Z., Bin Ramzan, M.A., Dhanya, C.T., Shukla, P., 2022. The role of global data sets for riverine flood risk Management at national scales. Water Resour. Res. 58, e2021WR031555. https://doi.org/10.1029/2021WR031555.
Bonatz, H., Reimann, L., Vafeidis, A.T., 2024. Comparing built-up area datasets to assess urban exposure to coastal hazards in Europe. Sci. Data 11, 499. https://doi.org/10.1038/s41597-024-03339-4.
Borrero, J.C., 2005. Field survey of northern Sumatra and Banda Aceh, Indonesia after the tsunami and earthquake of 26 december 2004. Seismol Res. Lett. 76, 312–320. https://doi.org/10.1785/gssrl.76.3.312.
BPS, 2024. https://bandaacehkota.bps.go.id/id/publication (Accessed 13 March 2024).
Bricker, J.D., Gibson, S., Takagi, H., Imamura, F., 2015. On the need for larger Manning's roughness coefficients in depth-integrated tsunami inundation models. Coast Eng. J. 57, 1550005. https://doi.org/10.1142/S0578563415500059, 1-1550005–13.
Bunya, S., Dietrich, J.C., Westerink, J.J., Ebersole, B.A., Smith, J.M., Atkinson, J.H., Jensen, R., Resio, D.T., Luettich, R.A., Dawson, C., Cardone, V.J., Cox, A.T., Powell, M.D., Westerink, H.J., Roberts, H.J., 2010. A high-resolution coupled riverine flow, tide, wind, wind wave, and storm surge model for southern Louisiana and Mississippi. Part I: model development and validation. Mon. Weather Rev. 138, 345–377. https://doi.org/10.1175/2009MWR2906.1.
Chen, W., Yao, T., Zhang, G., Li, F., Zheng, G., Zhou, Y., Xu, F., 2022. Towards ice-thickness inversion: an evaluation of global digital elevation models (DEMs) in the glacierized Tibetan Plateau. Cryosphere 16, 197–218. https://doi.org/10.5194/tc-16-197-2022.
Crawford, C.J., Roy, D.P., Arab, S., Barnes, C., Vermote, E., Hulley, G., Gerace, A., Choate, M., Engebretson, C., Micijevic, E., Schmidt, G., Anderson, C., Anderson, M., Bouchard, M., Cook, B., Dittmeier, R., Howard, D., Jenkerson, C., Kim, M., Kleyians, T., Maiersperger, T., Mueller, C., Neigh, C., Owen, L., Page, B., Pahlevan, N., Rengarajan, R., Roger, J.-C., Sayler, K., Scaramuzza, P., Skakun, S., Yan, L., Zhang, H.K., Zhu, Z., Zahn, S., 2023. The 50-year Landsat collection 2 archive. Science of Remote Sensing 8, 100103. https://doi.org/10.1016/j.srs.2023.100103.
Davies, G., 2019. Tsunami variability from uncalibrated stochastic earthquake models: tests against deep ocean observations 2006–2016. Geophys. J. Int. 218, 1939–1960. https://doi.org/10.1093/gji/ggz260.
Davies, G., Griffin, J., 2020. Sensitivity of probabilistic tsunami hazard assessment to far-field earthquake slip complexity and rigidity depth-dependence: case study of Australia. Pure Appl. Geophys. 177, 1521–1548. https://doi.org/10.1007/s00024-019-02299-w.
Devitt, L., Neal, J., Coxon, G., Savage, J., Wagener, T., 2023. Flood hazard potential reveals global floodplain settlement patterns. Nat. Commun. 14, 2801. https://doi.org/10.1038/s41467-023-38297-9.
Dusseau, D., Zobel, Z., Schwalm, C.R., 2023. DiluviumDEM: enhanced accuracy in global coastal digital elevation models. Remote Sensing of Environment 298, 113812. https://doi.org/10.1016/j.rse.2023.113812.
Fahrland, E., Paschko, H., Jacob, P., Kahabka, H., 2022. Copernicus DEM product handbook. https://dataspace.copernicus.eu/sites/default/files/media/files/2024-06/geo1988-copernicusdem-spe-002_producthandbook_i5.0.pdf.
Farr, T.G., Rosen, P.A., Caro, E., Crippen, R., Duren, R., Hensley, S., Kobrick, M., Paller, M., Rodriguez, E., Roth, L., Seal, D., Shaffer, S., Shimada, J., Umland, J., Werner, M., Oskin, M., Burbank, D., Alsdorf, D., 2007. The Shuttle radar topography mission. Rev. Geophys. 45, RG2004. https://doi.org/10.1029/2005RG000183.
Fukui, N., Mori, N., Miyashita, T., Shimura, T., Goda, K., 2022. Subgrid-scale modeling of tsunami inundation in coastal urban areas. Coastal Engineering 177, 104175. https://doi.org/10.1016/j.coastaleng.2022.104175.
Gayer, G., Leschka, S., Nöhren, I., Larsen, O., Günther, H., 2010. Tsunami inundation modelling based on detailed roughness maps of densely populated areas. Nat. Hazards Earth Syst. Sci. 10, 1679–1687. https://doi.org/10.5194/nhess-10-1679-2010.
GEBCO Bathymetric Compilation Group, 2023. The GEBCO_2023 Grid - a continuous terrain model of the global oceans and land. https://doi.org/10.5285/F98B053B-0CBC-6C23-E053-6C86ABC0AF7B, 2023.
Geiß, C., Schauß, A., Riedlinger, T., Dech, S., Zelaya, C., Guzmán, N., Hube, M.A., Arsanjani, J.J., Taubenböck, H., 2017. Joint use of remote sensing data and volunteered geographic information for exposure estimation: evidence from Valparaíso, Chile. Nat. Hazards 86, 81–105. https://doi.org/10.1007/s11069-016-2663-8.
Gesch, D.B., 2018. Best practices for elevation-based assessments of sea-level rise and coastal flooding exposure. Front. Earth Sci. 6, 230. https://doi.org/10.3389/feart.2018.00230.
Gibbons, S.J., Lorito, S., De La Asunción, M., Volpe, M., Selva, J., Macías, J., Sánchez-Linares, C., Brizuela, B., Vöge, M., Tonini, R., Lanucara, P., Glimsdal, S., Romano, F., Meyer, J.C., Løvholt, F., 2022. The sensitivity of tsunami impact to earthquake source parameters and Manning friction in high-resolution inundation simulations. Front. Earth Sci. 9, 757618. https://doi.org/10.3389/feart.2021.757618.
Giblin, J., Damlamian, H., 2022. Tsunami hazard assessment : Samoa case study (SPC technical report SPC00069). Pacific Community. https://www.spc.int/digitallibrary/get/a6x5z.
Gonzalez, C., Bueso-Bello, J.L., 2023. TanDEM-X 30m edited DEM product description. https://geoservice.dlr.de/web/dataguide/tdm30/pdfs/TD_GS_PS_0215_TanDEM_X_30m_Edited_DEM_Product_Description_v1_1.pdf.
Griffin, J., Latief, H., Kongko, W., Harig, S., Horspool, N., Hanung, R., Rojali, A., Maher, N., Fuchs, A., Hossen, J., Upi, S., Edi Dewanto, S., Rakowsky, N., Cummins, P., 2015. An evaluation of onshore digital elevation models for modeling tsunami inundation zones. Front. Earth Sci. 3. https://doi.org/10.3389/feart.2015.00032.
Grizonnet, M., Michel, J., Poughon, V., Inglada, J., Savinaud, M., Cresson, R., 2017. Orfeo ToolBox: open source processing of remote sensing images. Open geospatial data, softw. stand. 2, 15. https://doi.org/10.1186/s40965-017-0031-6.
Hawker, L., Bates, P., Neal, J., Rougier, J., 2018. Perspectives on digital elevation model (DEM) simulation for flood modeling in the absence of a high-accuracy open access global DEM. Front. Earth Sci. 6, 233. https://doi.org/10.3389/feart.2018.00233.
Hawker, L., Uhe, P., Paulo, L., Sosa, J., Savage, J., Sampson, C., Neal, J., 2022. A 30 m global map of elevation with forests and buildings removed. Environ. Res. Lett. 17, 024016. https://doi.org/10.1088/1748-9326/ac4d4f.
Hermosilla, T., Wulder, M.A., White, J.C., Coops, N.C., 2022. Land cover classification in an era of big and open data: optimizing localized implementation and training data selection to improve mapping outcomes. Remote Sensing of Environment 268, 112780. https://doi.org/10.1016/j.rse.2021.112780.
Hinkel, J., Feyen, L., Hemer, M., Le Cozannet, G., Lincke, D., Marcos, M., Mentaschi, L., Merkens, J.L., de Moel, H., Muis, S., Nicholls, R.J., Vafeidis, A.T., van de Wal, R.S.W., Vousdoukas, M.I., Wahl, T., Ward, P.J., Wolff, C., 2021. Uncertainty and bias in global to regional scale assessments of current and future coastal flood risk. Earth's Future 9. https://doi.org/10.1029/2020EF001882.
Huang, X., Song, Y., Yang, J., Wang, W., Ren, H., Dong, M., Feng, Y., Yin, H., Li, J., 2022. Toward accurate mapping of 30-m time-series global impervious surface area (GISA). Int. J. Appl. Earth Obs. Geoinf. 109, 102787. https://doi.org/10.1016/j.jag.2022.102787.
Iuchi, K., Takagi, H., Jibiki, Y., Kondo, T., Kusunoki, A., Hanifa, N.R., Pelupessy, D., Gayathri, R.T., Olshansky, R., 2023. Questioning the hazard map-based rebuilding process: learning from the 2018 Sulawesi earthquake in Indonesia. Coast Eng. J. 65, 126–148. https://doi.org/10.1080/21664250.2023.2165430.
Kaiser, G., Scheele, L., Kortenhaus, A., Løvholt, F., Römer, H., Leschka, S., 2011. The influence of land cover roughness on the results of high resolution tsunami inundation modeling. Nat. Hazards Earth Syst. Sci. 11, 2521–2540. https://doi.org/10.5194/nhess-11-2521-2011.
Koshimura, S., Oie, T., Yanagisawa, H., Imamura, F., 2009. Developing fragility functions for tsunami damage estimation using numerical model and post-tsunami data from Banda Aceh, Indonesia. Coast Eng. J. 51, 243–273. https://doi.org/10.1142/S0578563409002004.
Koshimura, S., Moya, L., Mas, E., Bai, Y., 2020. Tsunami damage detection with remote sensing: a review. Geosciences 10, 177. https://doi.org/10.3390/geosciences10050177.
Koyama, N., Yamada, T., 2022. Analysis of inundation characteristics under various computational conditions for large-scale flood forecasting. https://doi.org/10.5194/egusphere-egu22-10930.
Kulp, S.A., Strauss, B.H., 2018. CoastalDEM: a global coastal digital elevation model improved from SRTM using a neural network. Remote Sensing of Environment 206, 231–239. https://doi.org/10.1016/j.rse.2017.12.026.

Lachaise, M., Schweißhelm, B., 2023. TD-GS-PS-0216 TanDEM-X 30m DEM change maps product description. https://geoservice.dlr.de/web/dataguide/tdm30/pdfs/TD-GS-PS-0216_TanDEM-X_30m_DEM_Change_Maps_Product_Description_1.0.pdf.
Laso Bayas, J.C., Ekadinata, A., Widayati, A., Marohn, C., Cadisch, G., 2015. Resolution vs. image quality in pre-tsunami imagery used for tsunami impact models in Aceh, Indonesia. Int. J. Appl. Earth Obs. Geoinf. 42, 38–48. https://doi.org/10.1016/j.jag.2015.05.007.
Leach, N., Coops, N.C., Obrknezev, N., 2019. Normalization method for multi-sensor high spatial and temporal resolution satellite imagery with radiometric inconsistencies. Comput. Electron. Agric. 164, 104893. https://doi.org/10.1016/j.compag.2019.104893.
Li, J., 2017. Assessing the accuracy of predictive models for numerical data: Not r nor r2, why not? Then what? PLoS ONE 12, e0183250. https://doi.org/10.1371/journal.pone.0183250.
Li, B., Xu, X., Liu, X., Shi, Q., Zhuang, H., Cai, Y., He, D., 2023. An improved global land cover mapping in 2015 with 30 m resolution (GLC-2015) based on a multisource product-fusion approach. Earth Syst. Sci. Data 15, 2347–2373. https://doi.org/10.5194/essd-15-2347-2023.
Liao, M., Wen, H., Yang, L., Wang, G., Xiang, X., Liang, X., 2024. Improving the model robustness of flood hazard mapping based on hyperparameter optimization of random forest. Expert Syst. Appl. 241, 122682. https://doi.org/10.1016/j.eswa.2023.122682.
Liu, Y., Bates, P.D., Neal, J.C., Yamazaki, D., 2021. Bare-earth DEM generation in urban areas for flood inundation simulation using global digital elevation models. Water Res. 57. https://doi.org/10.1029/2020WR028516.
Lloyd, C.T., Chamberlain, H., Kerr, D., Yetman, G., Pistolesi, L., Stevens, F.R., Gaughan, A.E., Nieves, J.J., Hornby, G., MacManus, K., Sinha, P., Bondarenko, M., Sorichetta, A., Tatem, A.J., 2019. Global spatio-temporally harmonised datasets for producing high-resolution gridded population distribution datasets. Big Earth Data 3, 108–139. https://doi.org/10.1080/20964471.2019.1625151.
McClean, F., Dawson, R., Kilsby, C., 2020. Implications of using global digital elevation models for flood risk analysis in cities. Water Resour. Res. 56, e2020WR028241. https://doi.org/10.1029/2020WR028241.
Meilianda, E., Pradhan, B., Syamsidik, Comfort, L.K., Alfian, D., Juanda, R., Syahreza, S., Munadi, K., 2019. Assessment of post-tsunami disaster land use/land cover change and potential impact of future sea-level rise to low-lying coastal areas: a case study of Banda Aceh coast of Indonesia. Int. J. Disaster Risk Reduc. 41, 101292. https://doi.org/10.1016/j.ijdrr.2019.101292.
NASA JPL, 2020. NASADEM Merged DEM Global 1 arc second nc V001. https://doi.org/10.5067/MEASURES/NASADEM/NASADEM_NC.001.
Neuenschwander, A.L., Magruder, L.A., 2023. PhoREAL: increasing spatial and temporal data accessibly of ICESat-2 through open-source Python repository. In: Turner, M.D., Kamerman, G.W., Magruder, L.A. (Eds.), Laser Radar Technology and Applications XXVIII. Presented at the Laser Radar Technology and Applications XXVIII, p. 18. https://doi.org/10.1117/12.2667098. SPIE, Orlando, United States.
Neuenschwander, A.L., Pitts, K.L., Jelley, B.P., Robbins, J., Klotz, B., Popescu, S.C., Nelson, R.F., Harding, D., Pederson, D., Sheridan, R., 2023. ATLAS/ICESat-2 L3A land and vegetation height. Version 6. https://doi.org/10.5067/ATLAS/ATL08.006.
Neumann, T.A., Brenner, A., Hancock, D., Robbins, J., Saba, J., Harbeck, K., Gibbons, A., Lee, J., Luthcke, S.B., Rebold, T., 2023. ATLAS/ICESat-2 L2A global geolocated photon data. Version 6. https://doi.org/10.5067/ATLAS/ATL03.006.
Nosavan, J., Moreau, A., Hosford, S., 2020. SPOT World Heritage catalogue: 30 years of SPOT 1-to-5 observation (other). Oral. https://doi.org/10.5194/egusphere-egu2020-8275.
Pronk, M., Hooijer, A., Eilander, D., Haag, A., De Jong, T., Vousdoukas, M., Vernimmen, R., Ledoux, H., Eleveld, M., 2024. DeltaDTM: a global coastal digital terrain model. Sci. Data 11, 273. https://doi.org/10.1038/s41597-024-03091-9.
Sadashiva, V.K., Wang, X., Lin, S.-L., Lukovic, B., Heron, D.W., Suppasri, A., 2022. Quantifying effects of explicit representation of buildings in tsunami inundation simulations. Int. J. Disaster Risk Reduc. 81, 103277. https://doi.org/10.1016/j.ijdrr.2022.103277.
Scheffler, D., Hollstein, A., Diedrich, H., Segl, K., Hostert, P., 2017. AROSICS: an automated and robust open-source image Co-registration software for multi-sensor satellite data. Rem. Sens. 9, 676. https://doi.org/10.3390/rs9070676.
Schumann, G.J.-P., 2021. The full potential of EO for flood applications: managing expectations. In: Earth Observation for Flood Applications. Elsevier, pp. 305–320. https://doi.org/10.1016/B978-0-12-819412-6.00014-6.
Seeger, K., Minderhoud, P.S.J., Peffeköver, A., Vogel, A., Brückner, H., Kraas, F., Nay, Win Oo, Brill, D., 2023. Assessing land elevation in the Ayeyarwady Delta (Myanmar) and its relevance for studying sea level rise and delta flooding. Hydrol. Earth Syst. Sci. 27, 2257–2281. https://doi.org/10.5194/hess-27-2257-2023.
Sleeter, B.M., Wood, N.J., Soulard, C.E., Wilson, T.S., 2017. Projecting community changes in hazard exposure to support long-term risk reduction: a case study of tsunami hazards in the U.S. Pacific Northwest. Int. J. Disaster Risk Reduc. 22, 10–22. https://doi.org/10.1016/j.ijdrr.2017.02.015.
Sugawara, D., 2021. Numerical modeling of tsunami: advances and future challenges after the 2011 Tohoku earthquake and tsunami. Earth Sci. Rev. 214, 103498. https://doi.org/10.1016/j.earscirev.2020.103498.
Sugimoto, M., Iemura, H., Shaw, R., 2010. Tsunami height poles and disaster awareness: memory, education and awareness of disaster on the reconstruction for resilient city in Banda Aceh, Indonesia. Disaster Prev. Manag. 19, 527–540. https://doi.org/10.1108/09653561011091869.
Swanwick, R.H., Read, Q.D., Guinn, S.M., Williamson, M.A., Hondula, K.L., Elmore, A.J., 2022. Dasymetric population mapping based on US census data and 30-m gridded estimates of impervious surface. Sci. Data 9, 523. https://doi.org/10.1038/s41597-022-01603-z.
Tadono, T., Nagai, H., Ishida, H., Oda, F., Naito, S., Minakawa, K., Iwamoto, H., 2016. Generation of the 30 M-mesh global digital surface model by ALOS prism. Int. Arch. Photogramm. Remote Sens. Spatial Inf. Sci. XLI-B4, 157–162. https://doi.org/10.5194/isprs-archives-XLI-B4-157-2016.
Teluguntla, P., Thenkabail, P.S., Oliphant, A., Xiong, J., Gumma, M.K., Congalton, R.G., Yadav, K., Huete, A., 2018. A 30-m landsat-derived cropland extent product of Australia and China using random forest machine learning algorithm on Google Earth Engine cloud computing platform. ISPRS J. Photogrammetry Remote Sens. 144, 325–340. https://doi.org/10.1016/j.isprsjprs.2018.07.017.
Tiecke, T.G., Liu, X., Zhang, A., Gros, A., Li, N., Yetman, G., Kilic, T., Murray, S., Blankespoor, B., Prydz, E.B., Dang, H.-A.H., 2017. Mapping the world population one building at a time. https://doi.org/10.48550/ARXIV.1712.05839.
Tonini, R., Di Manna, P., Lorito, S., Selva, J., Volpe, M., Romano, F., Basili, R., Brizuela, B., Castro, M.J., de la Asunción, M., Di Bucci, D., Dolce, M., Garcia, A., Gibbons, S.J., Glimsdal, S., González-Vida, J.M., Løvholt, F., Macías, J., Piatanesi, A., Pizzimenti, L., Sánchez-Linares, C., Vittori, E., 2021. Testing tsunami inundation maps for evacuation planning in Italy. Front. Earth Sci. 9, 628061. https://doi.org/10.3389/feart.2021.628061.
Tsuji, Y., Tanioka, Y., Matsutomi, H., Nishimura, Y., Kamataki, T., Murakami, Y., Sakakiyama, T., Moore, A., Gelfenbaum, G., Nugroho, S., Waluyo, B., Sukanta, I., Triyono, R., Namegaya, Y., 2006. Damage and height distribution of Sumatra earthquake-tsunami of december 26, 2004, in Banda Aceh city and its environs. J. Disaster Res. 1, 103–115. https://doi.org/10.20965/jdr.2006.p0103.
U.S. Geological Survey, 2024. Earthquake Lists, Maps, and Statistics. accessed May 18, 2024 at URL. https://www.usgs.gov/natural-hazards/earthquake-hazards/lists-maps-and-statistics.
Wang, X., Power, W.L., 2011. COMCOT: a tsunami generation propagation and run-up model. GNS Science. Lower Hutt, New Zealand. GNS Science Report 2011/43 129 p.
Wu, L., Zhang, J., 2021. The effects of human movements on urban climate over Eastern China. npj Urban Sustain 1, 36. https://doi.org/10.1038/s42949-021-00038-6.
Yamazaki, D., Ikeshima, D., Tawatari, R., Yamaguchi, T., O'Loughlin, F., Neal, J.C., Sampson, C.C., Kanae, S., Bates, P.D., 2017. A high-accuracy map of global terrain elevations: accurate Global Terrain Elevation map. Geophys. Res. Lett. 44, 5844–5853. https://doi.org/10.1002/2017GL072874.
Yanagisawa, H., Koshimura, S., Miyagi, T., Imamura, F., 2010. Tsunami damage reduction performance of a mangrove forest in Banda Aceh, Indonesia inferred from field data and a numerical model. J. Geophys. Res. 115, 2009JC005587. https://doi.org/10.1029/2009JC005587.
Zeferino, L.B., Souza, L.F.T.D., Amaral, C.H.D., Fernandes Filho, E.I., Oliveira, T.S.D., 2020. Does environmental data increase the accuracy of land use and land cover classification? Int. J. Appl. Earth Obs. Geoinf. 91, 102128. https://doi.org/10.1016/j.jag.2020.102128.
Zheng, Y., Tang, L., Wang, H., 2021. An improved approach for monitoring urban built-up areas by combining NPP-VIIRS nighttime light, NDVI, NDWI, and NDBI. J. Clean. Prod. 328, 129488. https://doi.org/10.1016/j.jclepro.2021.129488.